



HAL
open science

Laser Ablation of a Terfenol-D (Tb_{0.3}Dy_{0.7}Fe_{1.92}) Microparticle Aerosol and Subsequent Supersonic Nanoparticle Impaction for Magnetostrictive Thick Films

Daniel O'Brien

► **To cite this version:**

Daniel O'Brien. Laser Ablation of a Terfenol-D (Tb_{0.3}Dy_{0.7}Fe_{1.92}) Microparticle Aerosol and Subsequent Supersonic Nanoparticle Impaction for Magnetostrictive Thick Films. Micro and nanotechnologies/Microelectronics. Ecole Centrale de Lille; University of Texas at Austin, 2007. English. NNT : . tel-00137712

HAL Id: tel-00137712

<https://theses.hal.science/tel-00137712>

Submitted on 21 Mar 2007

HAL is a multi-disciplinary open access archive for the deposit and dissemination of scientific research documents, whether they are published or not. The documents may come from teaching and research institutions in France or abroad, or from public or private research centers.

L'archive ouverte pluridisciplinaire **HAL**, est destinée au dépôt et à la diffusion de documents scientifiques de niveau recherche, publiés ou non, émanant des établissements d'enseignement et de recherche français ou étrangers, des laboratoires publics ou privés.

Copyright

by

Daniel Thomas O'Brien

2006

The Dissertation Committee for Daniel Thomas O'Brien
certifies that this is the approved version of the following dissertation:

**Laser Ablation of a Terfenol-D ($\text{Tb}_{0.3}\text{Dy}_{0.7}\text{Fe}_{1.92}$) Microparticle Aerosol and
Subsequent Supersonic Nanoparticle Impaction for Magnetostrictive Thick Films**

Committee:

Michael F. Becker, Supervisor

Philippe Pernod, Co-Supervisor

Gary Hallock

Mircea Driga

Vladimir Preobrazhensky

Jacque Teillet

**Laser Ablation of a Terfenol-D ($Tb_{0.3}Dy_{0.7}Fe_{1.92}$) Microparticle Aerosol and
Subsequent Supersonic Nanoparticle Impaction for Magnetostrictive Thick Films**

Publication No. _____

Daniel Thomas O'Brien, Ph.D.

The University of Texas at Austin,
l'Ecole Centrale de Lille et l'Université de Valenciennes
2006

Supervisor: Michael Becker
Co-Supervisor: Philippe Pernod

This dissertation describes using microparticles of the (giant) magnetostrictive material Terfenol-D ($Tb_{0.3}Dy_{0.7}Fe_{1.92}$) in the Laser Ablation of Microparticle (LAM) aerosols process for the generation of nanoparticles and their subsequent supersonic impaction to form nanostructured magnetostrictive thick films. Solid Terfenol-D was ground to a powder having diameters from 0.3 to 3 μm . This microparticle powder was then aerosolized and ablated by a KrF ultraviolet, pulsed laser in a continuously flowing aerosol process. The nanoparticles formed from the ablation were then accelerated

through a supersonic nozzle into vacuum where they impacted onto a substrate at room temperature forming a film. The nanoparticles were amorphous, as shown by x-ray diffraction analysis of the deposited films and by Transmission Electron Microscopy of individual particles, and had a size distribution typical of the LAM process: 3 to 20 nm in diameter with a mean size less than 10 nm.

The deposited films were characterized using the cantilever method to determine magnetostriction and elastic modulus. Values of magnetostriction were on the order of 15 ppm for LAM deposited films. The films were porous, due to their granular nature, reducing the elastic modulus to about 15 GPa. The reduced magnetostriction (1/30 that of comparable thin films) was due to oxidation. Spectroscopic analysis of the ablation plasma provided data in determining the source of the oxidation. Calculations showed that the extent of oxidation in the films was dependent on the microparticle feedstock size. For typical aerosol densities used in the LAM process, calculations showed that material made from microparticles having a diameter larger than 3 μm was not significantly affected by background gas impurities or by an oxide shell on the microparticles, whereas 0.3 μm diameter microparticles resulted in completely oxidized nanoparticles and hence films that were completely oxidized. From the behavior of the deposited films, the aerosolized microparticles had a mixture of diameters in between these two cases.

**Ablation Laser de microparticules de Terfenol-D ($Tb_{0.3}Dy_{0.7}Fe_{1.92}$) en aérosol et
dépôt supersonique des nanoparticules en résultant pour la fabrication de
films magnétostrictifs épais**

Cette thèse décrit la fabrication de couches épaisses nanostructurées magnétostrictives par dépôt supersonique de nanoparticules sur un substrat ; ces nanoparticules étant obtenues par le procédé d'Ablation Laser de Microparticules de Terfenol-D en aérosol. Un bloc solide de Terfenol-D a été réduit en poudre de microparticules de 0,3 à 3 μm de diamètre. Ces microparticules ont ensuite été injectées dans un aérosol s'écoulant en continu et ablaté par un laser ultraviolet KrF pulsé. Puis, les nanoparticules formées après l'ablation ont été accélérées par leur passage dans un micro-orifice. Le jet supersonique de nanoparticules en découlant a été utilisé pour déposer une couche épaisse sur un substrat à température ambiante. Les nanoparticules étaient amorphes, comme l'ont montré les analyses de diffraction aux rayons X des couches et les mesures de microscopie électronique à transmission (TEM) effectuées sur des particules individuelles. La distribution des tailles des nanoparticules était typique du procédé LAM : entre 3 et 20 nm de diamètre avec une moyenne de moins de 10 nm.

Les couches déposées ont été caractérisées par la méthode des poutres pour déterminer le module élastique et le niveau de magnétostriction. Les couches étant poreuses en raison de leur nature granulée, leur module élastique était réduit à environ 15 GPa. Le niveau de magnétostriction des couches était d'environ 15 ppm ; cette

magnétostriction réduite (1/30 de celui des couches fines) étant dû à un problème d'oxydation. Une analyse spectroscopique du plasma produit par l'ablation a permis la détermination de la source d'oxydation. L'étendue de l'oxydation des couches est apparue directement dépendante de la taille des microparticules utilisées initialement pour fabriquer les nanoparticules. Après calculs théoriques, pour des densités typiques d'aérosol utilisées dans le procédé LAM, il a été démontré que les nanoparticules fabriquées à partir de microparticules de plus de 3 μm de diamètre n'étaient pas affectées de façon significative par les impuretés présentes dans le gaz ou par l'oxydation de surface des microparticules. En revanche, les nanoparticules fabriquées à partir de microparticules de 0,3 μm de diamètre ou moins étaient, elles, oxydées et les couches en résultant l'étaient aussi. Experimentalement le diamètre des microparticules injectées en aérosol était présumé être entre ces deux cas.

Table of Contents

Abstract.....	iii
Abstract en Français.....	v
List of Tables.....	ix
List of Figures.....	x
List of Equations.....	xi
1 Introduction.....	1
1.1 Motivation.....	1
1.2 “Nano-”.....	3
1.3 Objectives.....	5
1.4 Organization.....	7
2 Magnetostriction.....	9
2.1 Definition.....	9
2.2 Terfenol-D.....	12
2.3 The Role of Nano.....	13
2.4 Oxidation.....	14
3 Laser Ablation of Microparticles (LAM).....	16
3.1 Laser Ablation of Microparticles.....	16
3.2 Nanoparticle Formation.....	19
3.3 Supersonic Impaction.....	21
3.4 LAM Applied to Terfenol-D.....	22
3.4.1 Process Parameters.....	22
3.4.2 Feedstock Microparticles.....	24
3.4.3 Nanoparticles from LAM of Terfenol-D.....	26
4 Measurement Apparatus and Techniques.....	29
4.1 The Cantilever Sample Geometry.....	29
4.1.1 Tip Deflection Measurement.....	29
4.1.2 Magnetostriction.....	32
4.1.3 Elastic modulus.....	34
4.1.4 Film Porosity (Density).....	36

4.2 Magnetic Field Source.....	37
4.2.1 Motivation.....	37
4.2.2 Background.....	38
4.2.3 Field Properties.....	43
4.4 Optical Emission Spectroscopy.....	47
5. Data and Analysis.....	52
5.1 Film Properties.....	53
5.1.1 Physical Appearance and Geometry.....	53
5.1.2 Elastic Modulus.....	55
5.1.3 Microstructure and Chemical Composition.....	60
5.1.4 Magnetization.....	65
5.2 Magnetostriction.....	66
5.3 Ablation Spectra.....	72
5.4 Data Summary.....	80
6 Discussion.....	81
6.1 Oxidation.....	82
6.1.1 Background Gas Impurities.....	82
6.1.2 Microparticle Surface Oxide.....	85
6.2 Future work.....	90
6.3 Conclusions.....	91
References.....	93
Vita.....	97

List of Tables

Table 1.1	Approximate number of atoms contained in an iron nanoparticle.....	4
Table 3.1	LAM process and deposition parameters.....	23
Table 5.1	LAM film composition data via EDS spanning 5 months.....	63
Table 5.2	Comparison of LAM/ PLD/ TbFe ₂ Film properties.....	67

List of Figures

Fig. 2.1	Schematic of volume and Joule magnetostriction.....	10
Fig. 3.1	LAM process illustration.....	18
Fig. 3.2	Microparticle breakdown cartoon.....	20
Fig. 3.3	SEM micrographs of Terfenol-D microparticles after milling.....	25
Fig. 3.4	TEM of Terfenol-D nanoparticles produced by LAM.....	27
Fig. 4.1	Schematic diagram of the cantilever tip deflection measurement.....	30
Fig. 4.2	Plot of elastic modulus vs. porosity.....	36
Fig. 4.3	Halbach array and cylinder config.; ideal and approximation.....	39
Fig. 4.4	Schematic of the rotation of the individual magnets for N=8 Mangle.....	42
Fig. 4.5	Magnetic field simulation minimum field strength configuration.....	44
Fig. 4.6	Magnetic field simulation maximum field strength configuration.....	45
Fig. 4.7	Magnetic field uniformity measurement.....	46
Fig. 4.8	Optical emission spectroscopy setup.....	48
Fig. 4.9	UV-VIS transmission spectra of OES red filter and quartz window.....	49
Fig. 4.10	Spectrum of a helium low pressure discharge showing impurities.....	50
Fig. 5.1	Photograph of LAM film.....	54
Fig. 5.2	Profilometry of LAM film.....	54
Fig. 5.3	Tip deflection vs. temperature hysteresis loops.....	56
Fig. 5.4	Tip deflection vs. temperature cooling curves only.....	57
Fig. 5.5	Plot of elastic modulus vs. porosity annotated for LAM films.....	58
Fig. 5.6	TEM of nanoparticles from LAM of Terfenol-D and copper.....	60
Fig. 5.7	SEM of film cross-section surface.....	61
Fig. 5.8	XRD of film and feedstock.....	62
Fig. 5.9	Bar chart of the EDS data of Table 5.1.....	64
Fig. 5.10	Magnetization hysteresis loops of a LAM film spanning 5 months.....	66
Fig. 5.11	Tip deflection vs. magnetic field curves for 4 different films.....	69
Fig. 5.12	Tip deflection vs. parallel and perp. magnetic field of LAM film.....	69
Fig. 5.13	Emission spectra of ablation of Terfenol-d microparticles.....	73
Fig. 5.14	Emission spectrum Terfenol-d microparticles with peaks identified.....	74
Fig. 5.15	Emission spectrum of ablation of solid Terfenol-D in air.....	76
Fig. 5.16	Time evolution of 777 and 845 lines of solid Terfenol-D in helium.....	78
Fig. 6.1	Oxygen ratio vs. microparticle diameter due to background impurities..	84
Fig. 6.2	Oxygen ratio vs. microparticle diameter due to surface oxide.....	86
Fig. 6.3	Total oxygen ratio vs. microparticle diameter.....	87

List of Equations

Eq. 4.1	Relation between tip deflection and displacement of a reflected beam...	31
Eq. 4.2	Calculation of magnetostriction from tip deflection.....	32
Eq. 4.3	Tip deflection as a function of magnetostriction, and other parameters..	32
Eq. 4.4	Magneto-elastic coupling coefficient.....	33
Eq. 4.5	Tip deflection of cantilever due to differences in coef. of thermal exp....	35
Eq. 4.6	Empirical relationship between elastic modulus and porosity.....	36
Eq. 4.7	Field strength inside an Halbach cylinder.....	40

1

Introduction

This dissertation is concerned with the application of the Laser Ablation of a Microparticle (LAM) aerosol process for the generation of nanoparticles and their subsequent supersonic impaction to form nanostructured thick films of the (giant) magnetostrictive material Terfenol-D ($\text{Tb}_{0.3}\text{Dy}_{0.7}\text{Fe}_{1.92}$). Hereafter, these films will be referred to simply as “LAM films.” Necessitated by this particular application, several methods and techniques, and the associated apparatus for analysis of the LAM process and deposited films are presented. This introduction chapter provides an overview of the motivation and objectives of the research and the organization of the following chapters.

1.1 Motivation

The research was motivated by a collaboration between Dr. M. Becker at the University of Texas at Austin (USA), and Professeur P. Pernod of Ecole Centrale de

Lille and the University of Valenciennes, Lille (France). The laser ablation of microparticle aerosols as a technique for the generation of nanoparticles was pioneered at UT under Dr. Becker and colleagues. Prof. Pernod and his colleagues at IEMN (Institut d'Electronique, Microélectronique, et Nanotechnologie) are experts in acoustics and magnetic materials, specifically magnetostrictive materials, for sensors and actuators on the MEMS (micro electro-mechanical systems) scale. Examples of MEMS devices are micro-valves, fluidic switches, deformable aerodynamic surfaces and mirrors, and directional ultrasonic transducer arrays for medical applications and non-destructive testing.

In most cases MEMS implies the use of thin films having thicknesses less than 5 micrometers. This is not usually by design, but due to the fact that thick films are technically difficult and impractical to fabricate using standard semiconductor manufacturing techniques (e.g., evaporation, sputtering, CVD, etc.); there are problems associated with internal stresses and thermal mis-match with the substrate, especially as films are often (necessarily) grown at elevated temperatures.

In addition, there exists a gap between thin films and the thicknesses that can be ground from bulk materials and then incorporated into devices. This gap is on the order of 5 to 100 micrometers which is the target thickness for a large fraction of MEMS devices. Supersonic jet deposition of nanoparticles generated by Laser Ablation of Microparticle (LAM) aerosols is capable of addressing exactly this thickness range of

films, as the process is done at room temperature and has the added features of a high deposition rate and direct-write ability.

1.2 “Nano-”

During the last 10 to 15 years the prefix “nano” has become common as a great deal of scientific might has been thrown at that particular size of mater, one to ten billionths of a meter in length where the behavior of material begins to shift from our normal everyday experience to the more quantum mechanical nature of its constituent atoms. Not only does this size range affect most properties of a material (e.g. melting point, hardness, conductivity, bandgap, etc.), but the effect is highly sensitive to changes in size and shape [1]. The possibility of controlling one or more of these metrics in order to tailor the behavior of the material has piqued the interest of most scientific and engineering disciplines.

In particular, the magnetic behavior of nanosized objects is of interest in this research. Magnetic systems are strongly affected by small grains or particle sizes. Grains sizes on the order of the magnetic domain wall thickness do not allow for domain wall movement. This requires any reorientation of the domain to be done by all of the magnetic dipoles acting as a unit. As this is much more energetically difficult, high coercivity magnets can be made from nanostructured materials. Conversely, for particle sizes much smaller than the characteristic magnetic length, soft magnetic

materials can be made, that in fact can become super-paramagnetic due to the ease with which the magnetization can be changed [2]. It is the magnetic softness of these small particles that is the property of interest for this work.

In general, the reactivity of materials increases as the size of the particle decreases. This is a result of the same mechanism that affects many of the other properties: the surface to volume ratio. For example, in a 1 nm diameter iron (Fe) particle, nearly all the atoms are surface atoms (cf. Table 1.1) with a few in the interior. This is from a simple geometric model using the density, molecular weight, and the length of a unit cell for crystalline iron. The values are only an approximation as the model assumes the bond length between the atoms is constant, though in fact, in such small particles it is no longer the case due to surface reconstruction and surface tension. However, from the model, it can be seen that for particles less than 10 nm in diameter, the surface to volume ratio becomes significant.

Table 1.1 Approximate number of atoms contained in an iron nanoparticle.

<i>Particle Diameter (nm)</i>	<i>Total Number of Atoms</i>	<i>Number of Surface Atoms</i>	<i>Percent Surface Atoms</i>
1	48	44	92
2	381	176	46
5	5,956	1100	18
10	47,647	4,398	9
20	381,180	17,593	5
50	5,955,936	109,956	2

Thermodynamically, the surface energy of a system is directly proportional to the surface area [3], and hence the surface energy becomes a significant fraction of the total energy of sub 10 nm particles. This high surface energy is the double-edged sword of nanoparticles. For example, the lowering of the temperature needed to sinter silver particles for use in high conductivity interconnects on plastic substrates [4], or the scrubbing of environmental contaminants from the air [5] are benefited by a higher surface energy and hence a more reactive nanoparticle. However, in the case of an iron–rare earth compound, such as Terfenol–D (an alloy of terbium, dysprosium, and iron), this reactivity is detrimental to the stability of the nanoparticles and the films made from them in terms of oxidation.

1.3 Objectives

The primary objective of the research presented in this dissertation, was to investigate the use of the LAM method of nanoparticle formation and subsequent supersonic nanoparticle impaction for the deposition of the magnetostrictive material Terfenol-D, and its (eventual) integration in the MEMS devices of IEMN. Hence, the author’s research time was split between UT and IEMN, although the project’s dependency on the LAM method, and its challenges, necessitated more time and research be done at UT. Unfortunately, integration of LAM films into MEMS devices was not achieved at the time of this writing.

Analysis of the initial deposited material, conducted at IEMN, showed only weak magnetostriction and thus forced the direction of research toward determining the cause and developing the ability to diagnose the LAM process and deposited films. The main challenges encountered, and those that are dealt with in this work, are the oxidation of the nanoparticles and the effect of porosity on the deposited film. Both serve to reduce, even prevent in the case of oxidation, the ability of the material to be used as an actuator/sensor.

Due to its oxygen sensitivity, the use of Terfenol-D in the LAM process for the production of magnetostrictive films was adapted (cooperatively with James Ma, fellow doctoral candidate) to an ultra-high vacuum (UHV) compatible system. That is to say that while the laser ablation part of the system takes place at one atmosphere of pressure of helium, not vacuum, the chamber and gas lines used metal seals and were subjected to rigorous cleaning procedures. UHV compatibility prevents oxygen or water vapor in the atmosphere from getting into the system, and allows the system to be baked at a higher temperature to more effectively drive off water from the inside surfaces after assembly. As a diagnostic tool in detecting the presence of oxygen, the author suggested and implemented spectroscopic observation and analysis of the plasma generated by the LAM process.

From the author's previous work with silver, it was known that the films made from supersonically impacting nanoparticles under the normal operating conditions of the LAM process, were porous and not fully dense. Additionally, the density was not

directly measurable and was hindered by the inability to accurately measure the film volume. In order to determine the elastic modulus of the film (an effect of porosity), the difference in the coefficients of thermal expansion of the film and substrate was exploited. This idea and the incorporation of a small oven in the magnetostriction measurement apparatus to measure the elastic modulus, was also the author's work.

Initially, film characterization in terms of magnetostriction was carried out at IEMN. After the focus of the research shifted more towards diagnosis and understanding of the LAM process itself, a magnetostriction diagnostic was needed at UT. Due to the negative influence on measurement resolution of the long settling time and induced temperature instability when using a large electromagnet, an alternative variable magnetic field source was sought. The solution was a novel magnetic field source constructed from permanent magnets that were articulated by mechanical gearing. The variable magnetic field source and magnetostriction measurement and data collection setup at UT were designed and built by the author. This reduced the validation time of LAM films and improved the sensitivity of the magnetostriction measurement.

1.4 Organization

The organization of the dissertation is similar to that of this introduction chapter. Chapter 2 follows with a detailed look at magnetostriction, Terfenol-D and the role of

nanometer length scales in its application as an actuator material. Chapter 3 begins the experimental part with a description of the LAM process: microparticle ablation, nanoparticle formation, and supersonic impaction into a film. Chapter 4 continues with a description of the apparatus that were built and the methods used to investigate the samples of LAM produced Terfenol-D films; specifically, optical emission spectroscopy of the ablation region, an uncommon variable magnetic field using only permanent magnets, and the use of the different coefficients of thermal expansion of the film and substrate, to give insight into the effect of reduced elastic modulus due to porosity in the film. Chapter 5 presents representative data that was collected using the methods and techniques of Ch. 4. Chapter 6 begins with a discussion of the source of oxygen in the films, suggests future work, and concludes the dissertation.

2

Magnetostriction

The one example of magnetostriction that is the most familiar whether it is known that it is due to magnetostriction or not, is the ubiquitous hum of transformers. The old fluorescent light starter transformers suffered from this as do roadside power transformers. The iron cores expand and contract with the changing magnetic field, and even though the physical change in size is small, 10 micrometers or less, it is enough to generate audible sound waves. This is more than just an annoyance as it is an electrical energy loss mechanism in the transformer and research is done to minimize it [6,7]. In this work however, a large magnetostriction is desirable, with the intent of converting electrical energy into useful mechanical work.

2.1 Definition

Magnetostriction is defined as a change in the dimension of a substance due to a change in its magnetic state. The first magnetostrictive phenomena encountered is “volume magnetostriction” where all three dimensions of a solid spontaneously change

in the same direction upon cooling below the magnetic ordering temperature (the Curie temperature) due to the magnetic ordering of the atoms in the solid. The second is the most commonly referred to property, called “Joule magnetostriction” after its discoverer W. P. Joule, and requires the presence of an external magnetic field. The associated change in dimension preserves volume, i.e., elongation in one direction is accompanied by contraction in the other two orthogonal dimensions (cf. Figure 2.1). It is the latter among other magneto-elastic effects, that is of interest in this work and will be referred to simply as magnetostriction.

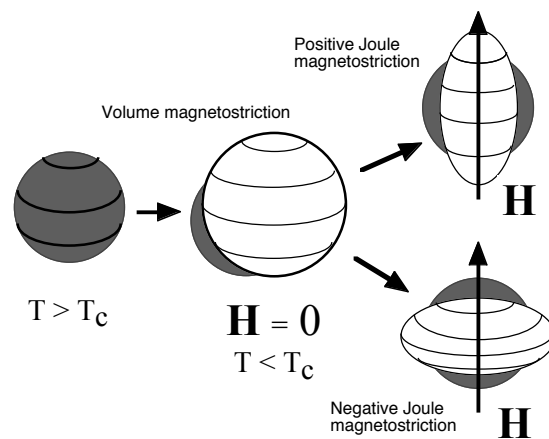


Figure 2.1 Schematic of volume and Joule Magnetostriction (after ref. [12])

The magnetostriction, λ , is defined as the ratio of the change in length to the total length, $\Delta L/L$, also known as strain, and is usually written with the dimensionless units of parts per million (ppm or 10^{-6}). Magnetostriction is a magneto-elastic coupling phenomenon between the classical elastic properties of a material and its quantum mechanical magnetic properties. Described simply, magnetism arises from the spin of

an electron, and in some part from the angular momentum of the electronic orbit around an atom. The elasticity of a material is due to how the electron orbits of neighboring atoms interact, i.e., how the constituent atoms bond together. Hence magneto-elastic coupling arises from the coupling between the direction of the spin of the electron and the orientation of its orbit. This is termed spin-orbit coupling and how strongly the spin and orbit are coupled, determines to what extent magnetic ordering of the solid (e.g., due to an external field) causes elastic deformation.

Spin-orbit coupling is present in all solids but is strongest in the rare-earth elements. This is due to the fact that the unpaired electrons that give rise to the magnetism of the atom, are located in the f orbit. This orbit is non-spherical and is much closer to the nucleus than the outer (s , p , and d) electron orbits. Hence, the electrons that occupy it do not participate in bonding between the atoms, and experience the nuclear attraction (more specifically the electric field gradient) to a larger extent. These conditions create a strong link between the spin of an electron and its orbit [8]. Hence, a change in the magnetic (spin) orientation causes a corresponding change in the orientation of the electron orbit. Because of the non-spherical orbit, this change in orientation results in an increase in the electrostatic interaction between it and neighboring electronic orbits. As this is an energetically unfavorable condition, the neighboring atoms move (an extraordinarily small amount of course) to accommodate the new orientation. The concerted motion of all the atoms in the solid creates a macroscopic change in dimension. This is magnetostriction.

2.2 Terfenol-D

The material with the highest magnetostriction is the rare-earth element, dysprosium, followed closely by terbium, with $\lambda \approx 9000 \times 10^{-6}$ though this is for extremely low temperatures, close to 0°K [9]. The reason terbium and dysprosium are not used by themselves for practical applications is that their Curie temperatures (magnetic ordering temperatures) are 220°K and 90°K, respectively, far below room temperature. Alloying the rare earths with transition metals results in an increase in the Curie temperature of the material, due to the longer range magnetic exchange interaction of the transition metal *d* orbitals. This helps to keep the rare earth atoms magnetically aligned above their normal curie temperature. Hence, the material with the highest *room temperature* magnetostriction, is single crystal TbFe₂ with $\lambda \approx 3600 \times 10^{-6}$. However, this material is highly anisotropic and has a large magneto-crystalline anisotropy energy, requiring fields on the order of 25 kOe in order to reach saturation and the maximum magnetostriction.

To overcome this, Terfenol-D, an inter-metallic alloy of terbium, iron (Fe), and dysprosium was created at the Naval Ordnance Laboratory in conjunction with the University of Iowa [10]. Dysprosium has the opposite sign of magneto-crystalline anisotropy energy (but the same sign of magnetostriction) as terbium, and so by substituting terbium with dysprosium, the magnetization becomes much easier and the coercivity decreases. Fields only as high as 1.5 kOe are needed to substantially saturate the material. The anisotropy energy is temperature dependent and so the amount of

dysprosium that is substituted is chosen such that the resulting anisotropy is a minimum at room temperature. This is important for practical applications and particularly necessary for MEMS devices where the driving coil size and available currents, and consequently the magnetic fields, are small.

2.3 The Role of Nano

In addition to the use of chemical composition to control the magnetic anisotropy, the crystal grain size of a material can influence the coercivity of polycrystalline soft ferromagnetic materials [11]. When the grain size is on the order of a hundred nanometers, corresponding to single domain particles, the material exhibits large coercivities. However, as the grain size becomes much smaller, on the order of nanometers, (smaller than about 10 nm for iron), the exchange interaction among the magnetic moments is much longer than the grain size and thus causes the moments to align even though the magnetization does not lie along any given grain's (easy) crystallographic direction. This gives long range magnetic order even over randomly oriented crystal grains and so reduces the crystalline anisotropy and coercivity of the material. Of course an amorphous system where even short range atomic order is suppressed, would be ideal in terms of minimizing the coercivity, though the magnetization and magnetostriction are reduced due to the fact that both are affected by the interatomic distances that tend on average to be larger in amorphous materials [12]. For example, polycrystalline TbFe₂ has a magnetostriction of ~2500 ppm at room

temperature (already lower than the single crystal magnetostriction) while amorphous TbFe₂ has a value of ~450 ppm [13].

In this work the starting feedstock material was Terfenol-D (Tb_{0.3}Dy_{0.3}Fe_{1.92}), as opposed to Terfenol (TbFe₂), simply due to the fact that Terfenol was not available for purchase. It would have been preferable to use the binary compound instead of the more complex ternary Terfenol-D, particularly in terms of analysis and comparison with current literature and for the interest in the improved anisotropy due to the nanoparticle size. However, the necessary time, equipment, and expertise to manufacture high quality TbFe₂ from individual terbium and iron, was beyond the scope of this research.

2.4 Oxidation

Oxidation of the magnetostrictive rare earth iron alloys has been investigated by various authors. In all cases, the inclusion of oxygen in the magnetostrictive material reduced the magnetostriction. Both Snodgrass, et al.[13] and Kim, et al.[14] measured the dependence of the magnetostriction coefficient for bulk Terfenol-D on oxygen, and arrived at a decrease in magnetostriction of 0.012 and 0.017 ppm per atomic ppm of oxygen, respectively. This was a linear dependence though it was measured only for values of oxygen impurities less than 7000 atomic ppm, corresponding to a 10 % decrease in magnetostriction from 1000 ppm in Kim, et al. The oxygen combines preferentially with the rare earth atoms, forming inclusions of R₂O₃ (R = rare earth) and leaving an iron-rich phase behind.

Quandt, et al.[15], and van Dover, et al.[16], both reported the spontaneous oxide growth on thin films having TbFe and TbDyFe compositions. The oxide layer was seen to grow more slowly over time for films containing a mixture of Tb and Dy, though films having the same rare earth content, but Tb only, started with a larger oxide thickness of about 25 nm as opposed to 15 nm. Van Dover, et al., indicated a segregated native oxide on TbFe₂ of 8 nm, consisting of a surface layer of 2 nm Fe₂O₃ and a sub-layer of 6 nm Tb₂O₃.

In general, most literature concerning thin films of magnetostrictive material do not report the effect of oxygen and oxidation on the films since after the initial oxide forms the oxidation rate is slow and confined to the surface. However, the initial oxide layer is typically reported to be 10 to 30 nm in thickness; as will be discussed in the following chapters, this oxide thickness is as large as or larger than the diameter of the nanoparticles generated by the LAM process. Should oxygen be present during the nanoparticle formation process or after formation but before impaction into a film, the nanoparticles would oxidize (possibly completely) and the oxygen would be incorporated homogeneously into the film. The susceptibility of the nanoparticles to oxygen prompted much of the research and investigative techniques described in this dissertation.

3

Laser Ablation of Microparticles (LAM)

The interaction of intense laser energy with matter has been studied since the demonstration of the first laser. Pulsed Laser Deposition (PLD), where a laser is focused onto a target such that material is ejected from the surface to be deposited on a nearby substrate, grew out of investigations into laser damage and has taken its place among magnetron and ion-beam sputtering and vacuum evaporation in the deposition of thin films. It is worth mentioning that all of the above techniques are capable of creating nanoparticles under certain conditions, though hitherto, such particles were generally considered contaminants and mainly served to degrade the quality of the thin film. This chapter introduces the ideas and apparatus behind one particular method of creating nanoparticles via laser ablation and the deposition of a film by their supersonic impaction.

3.1 Laser Ablation of Microparticles

A rather unconventional method for the production of nanoparticles using the interaction of lasers and microparticle aerosols originated at the University of Texas at

Austin about 12 years ago and applications of this process began in earnest with the LAM (Laser Ablation of Microparticles) patent of 1996 [17]. After preliminary investigations of ablating glass microparticles using a Nd:YAG laser [18], an ultraviolet KrF laser was employed for ablation, and the list of materials studied was broadened to include various metals, ceramics, and semiconductors. Initial experimentation of ablating microparticles dispersed on quartz plates was followed by the design of a flowing aerosol process [19]. A schematic diagram of the current LAM system (with deposition of the nanoparticles by supersonic impaction) is shown in Fig. 3.1.

In the aerosol LAM process, an aerosol of microparticles, ideally having diameters on the order of a few micrometers, is confined in a laminar flow by a sheath gas and passes through the focus of a pulsed ultraviolet (UV) laser. The gas flow speed is such that new microparticles are ablated with each shot (and theoretically none are missed) forming a continuous nanoparticle aerosol. This nanoparticle aerosol is directed through a virtual impactor assembly to separate any unablated microparticles from the gas stream. The separate nanoparticle stream is accelerated through a nozzle into vacuum where the nanoparticles impact upon a substrate. In order to create films, the substrate is translated in a closely spaced X-Y raster pattern, thus depositing overlapping lines of nanoparticles.

(a) Raw material feed

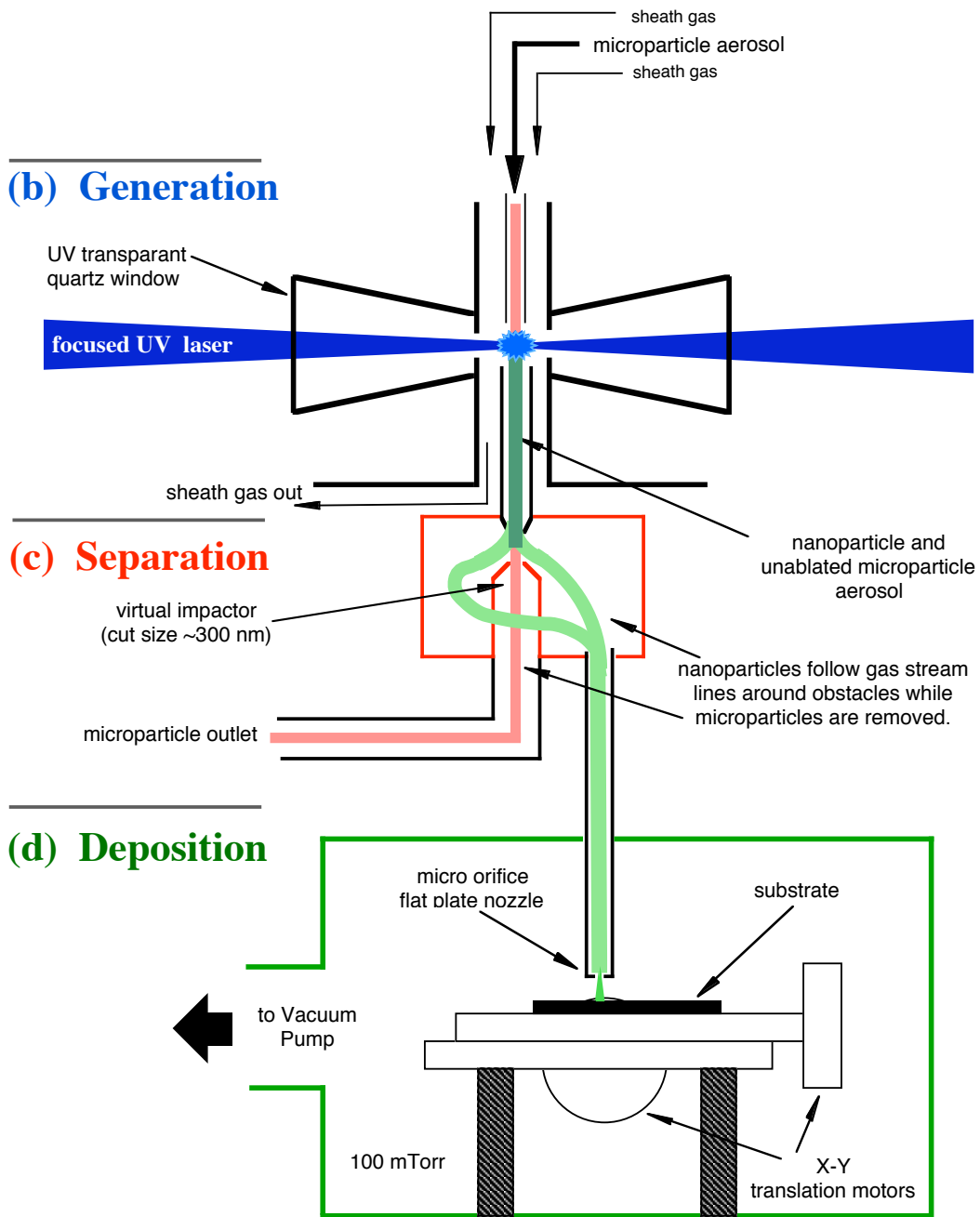


Figure 3.1 Illustration of the LAM system for nanoparticle production and deposition of nanoparticulate films. (a) microparticle aerosol input (b) transformation of starting micron sized powder to nanoparticles via laser ablation (c) separation of nanoparticles from larger material (d) deposition of nanoparticles via supersonic impaction.

3.2 Nanoparticle Formation

LAM employs a distinctly non-equilibrium process for the formation of nanoparticles. As shown by Lee, et al. using nanosecond time-scale Schlieren imagery and numerical modeling, the laser-microparticle interaction is a violent, albeit localized process, having high velocities (thousands of meters per second), high temperatures (tens of thousands of Kelvin electron temperature), and short time scales (tens of nanoseconds) [20]. Figure 3.2 shows a cartoon of the events of microparticle ablation for metallic materials. Initially, the microparticle is irradiated by the laser where surface absorption occurs within the skin depth. For Terfenol-D and the laser wavelength of 248 nm used in these experiments, the skin depth is on the order of 10 nm. This layer is explosively heated to a plasma, and a shockwave is sent through the core of the microparticle. As the shockwave travels through the particle, it compressively heats and vaporizes the bulk, which then condenses in the low-pressure region behind the shockwave, forming particles of nanometer dimensions.

As described by Nichols, et al., nanoparticles that are produced from metals have a bimodal size distribution [21]. Through a series of experiments, the authors attributed this to two methods of formation. The first mode of smaller diameter particles was assigned to those nanoparticles that form behind the shockwave. The second mode containing larger sized particles was assigned to particle formation from the vapor ejected during the initial heating and evaporation of the surface layer before the shockwave was initiated.

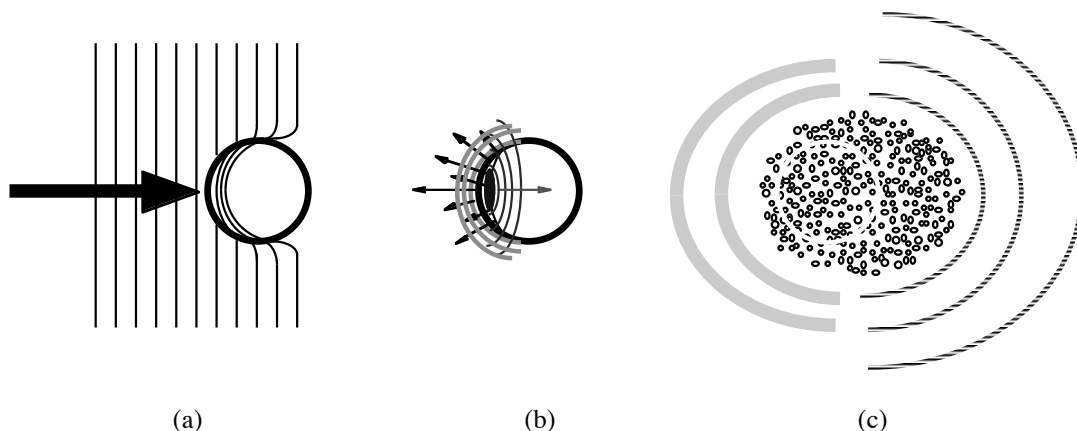


Figure 3.2 Cartoon showing the different stages of laser irradiation and microparticle breakdown. (a) plane wave illumination and skin depth absorption (b) plasma explosion at front surface and the launching of a shockwave through the particle (c) expansion of initially evaporated material from the front of the microparticle, nanoparticle condensation behind the shockwave, and exit of shock from initial particle area.

The size distribution of silver nanoparticles was studied extensively by Nichols, et al. for different parameters of the LAM process, e.g. laser fluence, initial feedstock microparticle size, and background gas pressure. For the same parameters used in this work with Terfenol-D, particularly ablation in 1 atm of helium, the distribution of silver nanoparticles showed a mean diameter of 8 nm and had a dispersion of about 70%. Due to the fact that Terfenol-D has a similar skin depth (10 nm) to that of silver (3 nm), it was expected that the resulting nanoparticles would have a similar size range and distribution. This was verified qualitatively by Transmission Electron Microscopy (TEM), and is discussed later in section 3.4.3.

3.3 Supersonic Impaction

The collection of aerosolized nanoparticles is difficult. Because they have such small mass and large surface area, the gas around them appears viscous and they tend to follow gas streamlines around objects. In order for such particles to move against the gas, e.g. to cross streamlines, there needs to be a force greater than the drag of the gas. Being a weak force, gravity has essentially no effect on the motion of the nanoparticles. Electrostatic collection, i.e. use of the force of an electric field, is one possibility if the nanoparticles are charged. Thermophoresis can also provide a collection force; there is a pressure gradient from a hot surface to a cold surface that will drive the nanoparticles to the cold surface where they are adsorbed. In this work, acceleration of the particles to a high speed through a nozzle is used, resulting in ballistic impaction upon a surface. The kinetic energy is transformed on impaction into deformation of the particle (and possibly the substrate) and heat [22]. This has the effect of improving the density and adherence of the particles to the substrate as well as to each other.

Acceleration of the particles is accomplished by directing the nanoparticle aerosol through a micro-orifice (0.2 to 0.3 mm in diameter) from atmospheric pressure into vacuum (~ 100 mTorr), a pressure ratio of ~ 7000 . The gas is accelerated across the pressure drop, accelerating the nanoparticles with it.

Recently Huang, et al. have modeled the aerosol gas dynamics in the nozzle, nanoparticle acceleration in the jet, and silver nanoparticle deposition by impaction onto a substrate for both a flat plate orifice and a conical nozzle [23]. The authors found that

the resulting film morphology was highly dependent on nanoparticle impaction energy. The highest film densities were obtained using helium and a conical nozzle. Modeling of the jet showed helium attained the highest exit velocity of the gases studied, He, Ar, and N₂. The use of a conical nozzle, did not significantly change the exit velocity of the carrier gas, but did increase the ability of the gas to accelerate the nanoparticles by lengthening the effective nanoparticle acceleration region. This increased their exit velocity by roughly 200 m/s. Final impaction energies were calculated to be 0.6 eV/atom for 10 nm diameter silver particles having an impaction velocity of around 1000 m/s. Impaction energies less than 0.25 eV/atom are considered soft landings and preserve the original nanoparticle morphology. Molecular Dynamics (MD) simulations suggest impaction energies greater than 1 eV/atom are necessary for fully dense film formation [24]. Helium and a conical nozzle were used in the deposition of nanoparticles in this work on Terfenol-D in order to have as high a density of the films as possible with the current system.

3.4 LAM Applied to Terfenol-D

3.4.1 Process Parameters

The LAM apparatus was operated in a fashion similar to previous work with other materials, most notably silver. Table 3.1 summarizes the various process parameters of the setup. The laser fluence, determined by the focal area, beam energy,

and energy loss of the optics, was greater than or equal to 2 J/cm², above the breakdown threshold for silver and other metals. The repetition rate was chosen to coincide with the focal volume and flow rate of the microparticle aerosol, such that a new volume of aerosol was ablated with each laser shot with a slight overlap to minimize unablated particles at the edge of the laser focus.

Table 3.1 Process parameters for sample manufacture

Laser –	KrF Excimer (Lumonics 848)
– Wavelength / photon energy	248 nm / 5 eV
– Energy	200 mJ/pulse
– Fluence	≥ 2 J/cm ²
– Pulse length	15 ns
– Repetition rate	170 pps (pulses per second)
Feedstock microparticles	milled Terfenol-D from Etrema, Inc.
Carrier gas type	helium (ultra-high purity) 99.999%
Microparticle aerosol flow	120 sccm
Sheath flow	1300 sccm
Pressure in ablation region	760 Torr (one atmosphere)
Pressure in deposition chamber	100 mTorr (He)
Substrate speed	1 mm/s
Nozzle to substrate distance	~ 5 mm
Nozzle (conical)	0.25 mm throat, 30° cone angle, 0.8 mm exit
Substrate material	silicon, glass, or plastic (Mylar)
Substrate thickness	150 to 250 μ m
Deposition temperature	25 °C (room temperature)

The nozzle that was used to accelerate the particles to sufficient energies to impact upon the substrate was a conical nozzle having a throat diameter of 0.25 mm and a 30° full angle diverging section 2 mm long. A distance from the nozzle to the

substrate of about 5 mm was typical. Vacuum in the deposition chamber was achieved by the concerted effort of a roots blower feeding an Edwards 40 vacuum pump. These two as a unit were capable of maintaining vacuum at 100 mTorr while the nozzle was operating with a stagnation pressure of 1 atm upstream. These conditions, i.e., a small orifice, high pressure ratio, and short nozzle-substrate distance, allow the system to be well described by the model of Huang, et al. (cf. section 3.3). Helium was chosen as the working gas for all samples in order to increase the nanoparticle impaction velocity and hence the density of the deposited films.

3.4.2 Feedstock Microparticles

The starting raw material was Terfenol-D ($\text{Tb}_{0.3}\text{Dy}_{0.7}\text{Fe}_{1.92}$) purchased from Etrema, Inc. (USA) in the form of a solid rod and plate. Inside a glove box in an inert argon atmosphere, small sections were broken off the rod and pulverized using a ball mill with tungsten carbide milling balls, or ground by hand using a ceramic mortar and pestle. Terfenol-D is extremely brittle and was easy to fracture and grind into a powder. The powder was then sifted through two meshes having hole sizes of 100 μm and 30 μm . Figure 3.3 shows SEM micrographs at different magnifications of the resulting powder after being dispersed onto a silicon substrate. Of note is the fact that there is a large size distribution with micron-sized agglomerates made up of sub-micron particles having diameters as low as 300 nm. The microparticles necessarily were exposed to air in the transfer between the glove box and SEM. Normal operating procedure for the

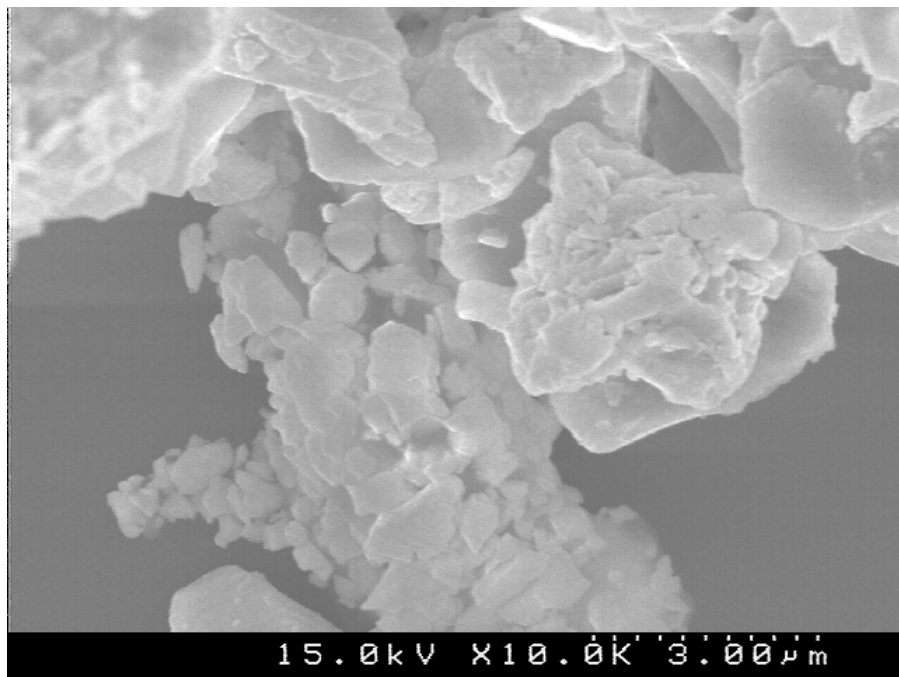
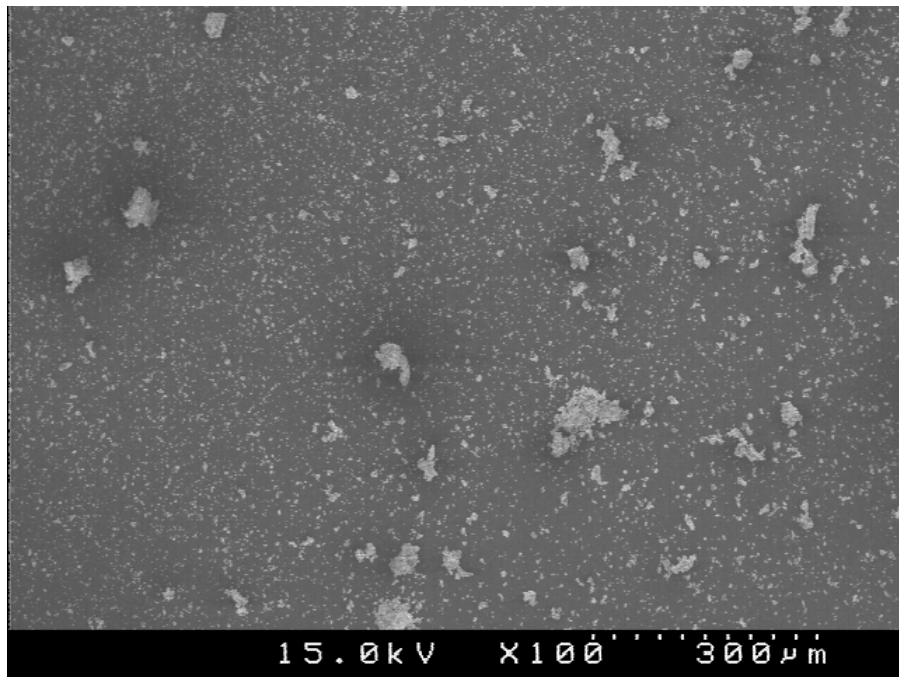


Figure 3.3 SEM micrographs of Terfenol-D microparticles after milling.

LAM process is to seal the microparticles in the aerosolizer while still in the glove box, for transport and connection to the laser ablation cell.

3.4.3 Nanoparticles from LAM of Terfenol-D

From previous work on silver and other materials, it is known that the nanoparticles that are generated from LAM are typically from 3 to 20 nm with a peak in the size distribution below 10 nm in diameter. TEM grids (small copper meshes covered by a 10 nm thick layer of carbon film) were exposed to the supersonic jet of nanoparticles for a few seconds to obtain a sample of the impacting nanoparticles for analysis in the TEM (Transmission Electron Microscope). Figure 3.4 shows two micrographs from such grids. In the top image, the region is of dense nanoparticles, just as the deposit begins to become a film. From this and other low magnification images it is possible to say that the particle size distribution from laser ablation of Terfenol-D microparticles is not overly different from other materials used with the LAM process. The bottom image is at a higher magnification, showing a single particle on the order of 15 nm in diameter with an amorphous structure that is indistinguishable from the amorphous carbon background layer. Similar to the SEM micrographs, the particles were exposed to air while transferring the sample grids to the TEM. Hence it is assumed that what are pictured are either partially or completely oxidized particles. Elemental analysis using the TEM indicated that small groups of nanoparticles, the

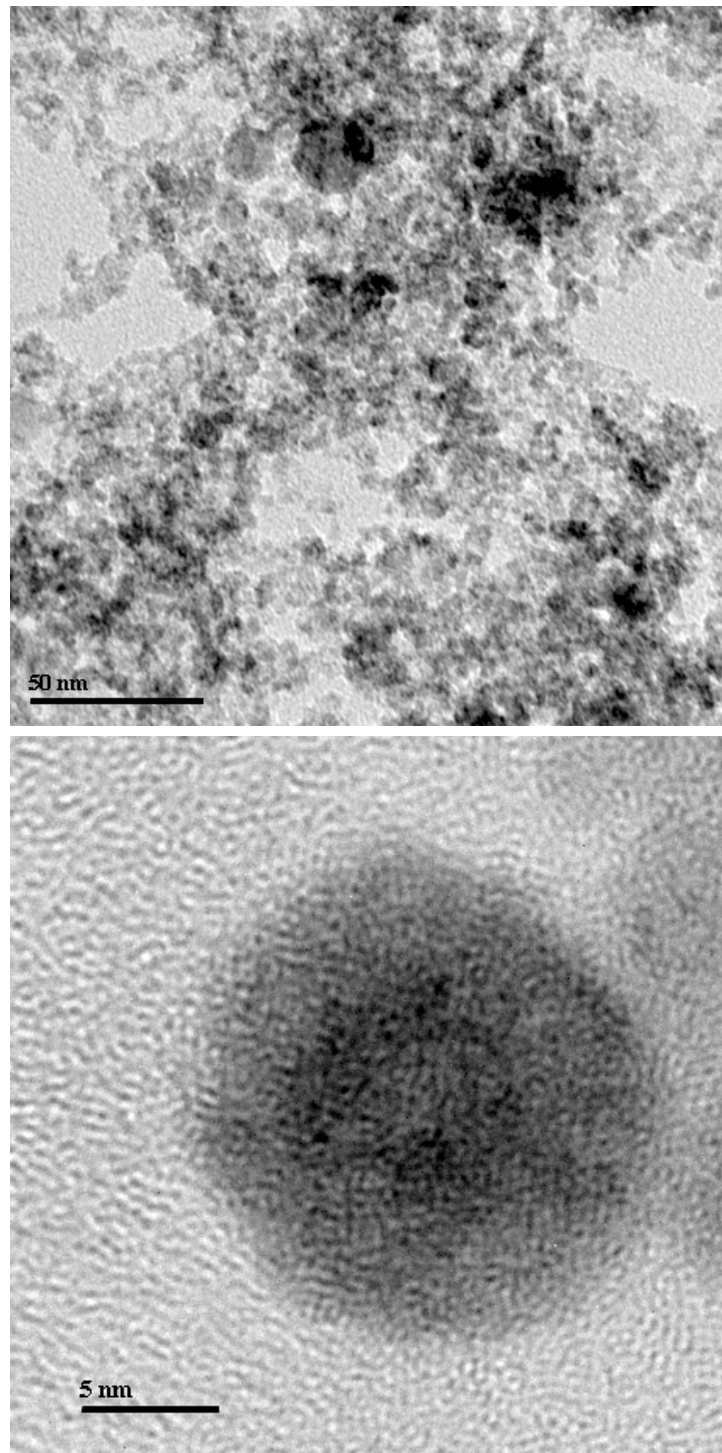


Figure 3.4 High Resolution Transmission Electron Microscopy (HRTEM) of nanoparticles made via the LAM process from Terfenol-D microparticles. (top) First stages of film growth via supersonic impactation of individual nanoparticles and (bottom) an individual nanoparticle showing amorphous structure.

highest resolution possible for the analysis, contained all three elements, Tb, Dy, and Fe of the starting Terfenol-D microparticles.

The next chapter continues the experimental setup with a description of the methods and techniques that were developed to analyze the films created with the LAM method and to diagnose the presence of oxygen in the ablation plasma.

4

Measurement Apparatus and Techniques

This chapter describes the methods and techniques that were used to analyze the deposited films. The use of samples (films deposited on substrates) in the form of cantilevers, provided a means to measure the elastic modulus (and hence porosity) and magnetostriction of the films. The novel magnetic field source used in the magnetostriction measurement and the use of optical spectroscopy for the detection of oxygen in the laser ablation and nanoparticle formation region are described as well as.

4.1 The Cantilever Sample Geometry

4.1.1 Tip Deflection Measurement

The method of choice for measuring the magnetostriction of the LAM films is one of the most common ways: the cantilever. A long narrow sample consisting of two layers, a substrate and the film in question, is fixed at one end and the deflection (bending angle) of the free end is measured while an external parameter is varied. The

deflection is due to different changes in length (strain) of the film and substrate. In this case, it is the application of a magnetic field or a change in temperature that causes the changes in length and the beam to deflect. This principle is the basis for bimetallic thermostats and automobile turn signals (before the solid state variety). Consider Fig. 4.1 that shows the bending of a cantilever due to an applied magnetic field. If the film is magnetostrictive (and the substrate is non-magnetic or has a different magnetostriction coefficient), the cantilever will bend due to the film expanding or contracting while the substrate does not (or does to a different degree). Typically the beam also experiences a torque about the long axis.

There are many ways to measure the deflection of the cantilever (capacitance, inductance, visual inspection, etc), however one of the most sensitive and easiest to implement is by measuring the displacement of a beam of light (usually a laser) reflected off the end of the cantilever.

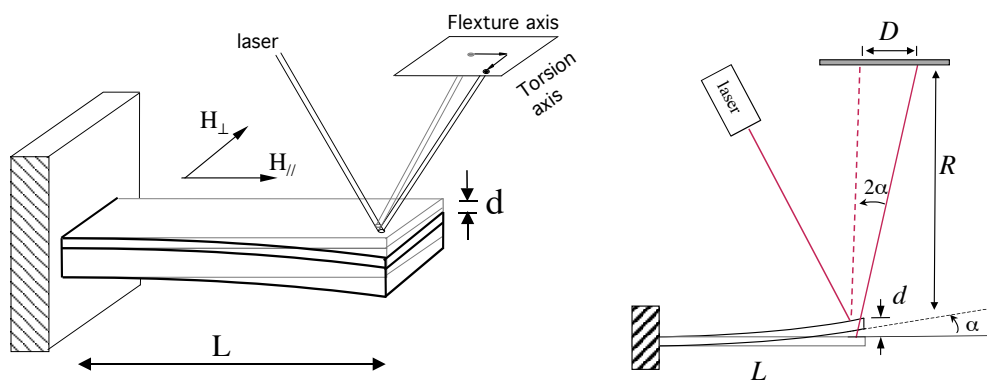


Figure 4.1 Schematic diagram of the cantilever tip deflection calculation via measurement at the detector of the motion of a reflected laser beam off the cantilever tip.

This method also has the advantages of not requiring contact with the cantilever and simply moving the sensor farther away from the cantilever increases the resolution of the measurement. This is because the tip deflection is due to the bending of the cantilever, creating an angle between the tangent line at the tip when bending and that when in the original resting position. Hence, for a given angle, the distance swept by that angle is dependent on the radial distance away from the bending point. Of course the signal to noise ratio remains the same, regardless of the distance.

Looking at Fig. 4.1, for small angles, $\tan(\alpha) \approx \alpha$, and so the tip deflection d is a function of the linear displacement of the beam D at the detector a distance R away from the cantilever, which has length L , and is written,

$$d = \frac{LD}{2R} . \quad (4.1)$$

At IEMN, the detection of the reflected laser spot was done with a 2-D Position Sensitive Diode (PSD) that allowed the simultaneous measurement of flexural and torsional bending of the cantilever. At UT, a single axis PSD was used to measure only the flexure of the cantilever. The distance between the cantilever tip and the PSD was typically 1 meter, and with a 12 bit A/D converter, this allowed resolutions on the order of 10 nanometers of tip displacement for a 10 millimeter long cantilever. In addition, a Hall effect probe or a thermocouple was situated in close proximity to the cantilever to measure the independent variable, magnetic field or temperature respectively.

4.1.2 Magnetostriction

The relationship between magnetostriction and cantilever tip deflection is given by

$$\lambda = -\frac{2}{9} \frac{d_{\parallel} - d_{\perp}}{L^2} \frac{E_s}{E_f} \frac{h_s^2}{h_f} \frac{(1 + \nu_f)}{(1 + \nu_s)}, \quad (4.2)$$

where λ_s is the saturation magnetostriction of the film, d_{\parallel} is the tip deflection with the magnetic field applied parallel to the cantilever long dimension, d_{\perp} is the tip deflection with the magnetic field applied perpendicular (and in-plane) to the cantilever long dimension, L the cantilever length, h the thickness, E the elastic (Young's) modulus, and ν Poisson's ratio, with subscripts s and f denoting substrate and film respectively [25].

The derivation of Eq. (4.2) assumes that the substrate is not magnetically influenced, the film has a thickness much smaller than the substrate, and the cantilever has a length large compared to its width and much larger than its thickness. The cantilevers in this work were approximately 10 mm long and 2 to 4 mm wide, the substrate was silicon, glass, or plastic, of thicknesses around 200 μm , and the films were between 1 and 10 μm thick. Hence the assumptions are valid for these conditions and the equation is applicable. The film is assumed to cover the entire substrate.

For diagnostic purposes, it can be easier to think in terms of the observable, that being the tip deflection of the cantilever, and rewrite Eq. (4.2) as

$$d_{\parallel} - d_{\perp} = -\frac{9}{2} \lambda L^2 \frac{E_f}{E_s} \frac{h_f}{h_s} \frac{(1 + \nu_s)}{(1 + \nu_f)}. \quad (4.3)$$

The tip deflection is proportional to the magnetostriction, the film thickness, and the elastic modulus of the film. While the film thickness is directly controllable, the magnetostriction and elastic modulus are not. Hence, these are properties of the film that require investigation, particularly when the material does not perform as expected. In this case, the relevant dependencies of these parameters are: 1) magnetostriction is a function of chemical composition, oxidation or contamination, and film microstructure, i.e., whether it's amorphous, nanocrystalline, polycrystalline or single crystal, and 2) the elastic modulus is a function of porosity (density) of the material. Poisson's ratio, ν , does not depend strongly on these variables and is assumed to be constant throughout. While magnetostriction is not dependent on magnetization, per se, magnetization is a good indicator as to the ability of the material to react to a magnetic field and depends upon the same material properties as described above. Representative magnetization, composition, and microstructure data for the LAM films are presented in Chapter 5.

The magnetoelastic coupling coefficient, b , is suggested by Trémolet, et al.[25] to present thin film data as opposed to the magnetostriction λ , and is defined as

$$b = \frac{1}{6} \frac{(d_{\parallel} - d_{\perp})}{L^2} \frac{h_s^2}{h_f} \frac{E_s}{(1 + \nu_s)}. \quad (4.4)$$

This parameter describes how much stress the film is able to apply to the system and has units of pressure (e.g. MPa). It has the advantages that it does not include the elastic modulus of the film in the calculation (often an unknown for thin films) and is a

more “practical device” figure of merit than a material property. Magnetostriction data presented in Chapter 5 are displayed using both units of measure.

4.1.3 Elastic Modulus

Since it was known that films made from supersonically impacted nanoparticles using the current LAM system are not fully dense (which decreases the elastic modulus and the ability of the material to apply a force to the substrate), the cantilever geometry was applied to determine the elastic modulus as well. This was calculated from the effect of temperature on the curvature of a film-on-substrate cantilever due to differences in their respective coefficients of thermal expansion. It was then used as an independent measurement of porosity.

The tip deflection of the cantilever was measured using the same setup as was used to measure the tip deflection of the cantilever due to a magnetic field, with the difference that the magnet assembly was replaced with a small oven and the Hall probe with a thermocouple. A change in temperature of 5°C was completely sufficient to measure tip deflections on the order of 150 nm. At the time of the measurement this was twice the maximum deflection of LAM films due to a magnetic field. The measurement resolution was of the order of 0.005°C difference from ambient and 10 nm of tip displacement.

Due to the possible influence of the magnetic field from the heater element, the curve of tip deflection vs. temperature was taken as the oven cooled after turning off the

heater current. Without active temperature stabilization, the oven must have a lower thermal conductivity than either the thermocouple tip or cantilever such that the thermocouple and cantilever can be said to be at the same temperature. This condition can be verified by the amount and symmetry of the hysteresis in the tip deflection vs. temperature curve as the dependence ideally should be linear.

The tip deflection of a cantilever due to a difference in coefficients of thermal expansion between the film and substrate was described for bimetallic thermostats [26] and more recently analyzed considering the case where the film and substrate have different widths [27]. The published equation of [27] is rewritten using the same variable symbols used for the calculation of magnetostriction, with the addition of width, w , as:

$$d = \frac{L^2}{2} \frac{6 w_s w_f E_s E_f h_s h_f (h_s + h_f) (\alpha_f - \alpha_s)}{(w_s E_s h_s^2)^2 + (w_f E_f h_f^2)^2 + 2 w_s w_f E_s E_f h_s h_f (2h_s^2 + 3h_s h_f + 2h_f^2)} \Delta T . \quad (4.5)$$

Here again, subscripts s and f denote substrate and film respectively. ΔT is the temperature difference between measurements, d is the tip deflection of the cantilever, L the cantilever length, h the thickness, E the elastic modulus, and α the coefficient of thermal expansion. It is the slope of the acquired tip deflection vs. temperature curve that is used in the calculation to obtain the elastic modulus of the film.

4.1.4 Film Porosity (Density)

After obtaining the elastic modulus, it is possible to calculate the porosity of the deposited film. The empirical relationship,

$$E_{eff} = E_{bulk}(1 - \varepsilon)^{3.4} \quad (4.6)$$

was derived from a curve fit of data for various sintered iron compounds [28]. E_{eff} is the effective elastic modulus, E_{bulk} is the elastic modulus of the bulk (non particulate) material, and ε is the fractional porosity (hence $(1-\varepsilon)$ is the fractional density).

Figure 4.2 is a plot of fractional elastic modulus E_{eff}/E_{bulk} vs. fractional porosity ε from Eq. (4.6).

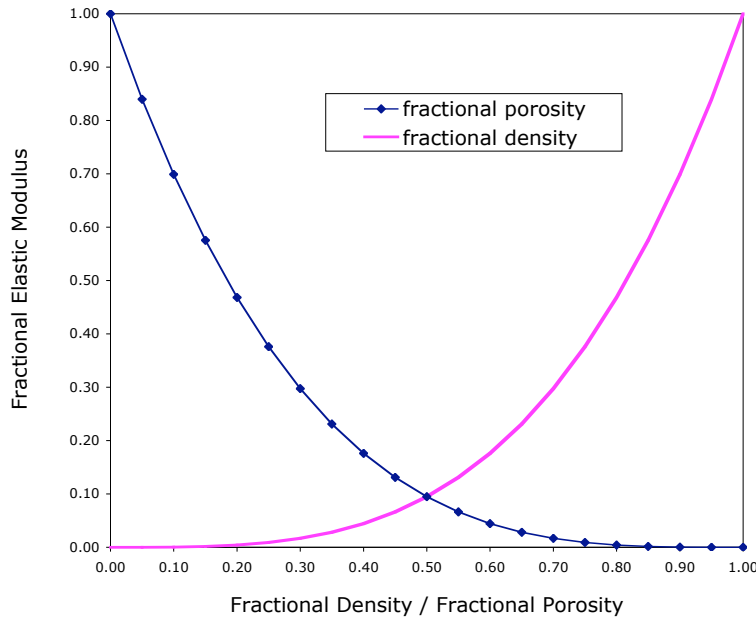


Figure 4.2 The dependence of elastic modulus on porosity(density) from the empirical model of McAdam et al,[28] for various particle compacts of iron compounds.

Of note is how quickly the elastic modulus drops for small fractional porosities. A fractional porosity of 0.2 results in an effective elastic modulus half that of the bulk modulus. Consequently, the tip deflection of a cantilever due to the magnetostriction of a film that is 20% porous will be reduced by half as well (cf. Eq. (4.3)).

4.2 Magnetic Field Source

4.2.1 Motivation

The magnetic field source used at IEMN in France was an air-cooled electromagnet with an iron core. It was routinely used to produce magnetic fields up to 2600 Oe (at 8.6 Amperes). To prevent the room lights and sunlight from interfering with the detection of the laser spot by the PSD and to reduce the variations in temperature due to sunlight, the measurement apparatus was surrounded by a heavy curtain on the sides and household aluminum foil on the top. One of the drawbacks of such an electromagnet is the extremely large inductance it represents. This necessitates a long (few seconds) settling time for the driving current. To record a full hysteresis loop at a nominal magnetic field strength resolution, the complete measurement took about 40 minutes. During this time, the temperature of the environment around the electromagnet increased a few degrees Centigrade and caused the measured deflection to drift due to the different coefficients of thermal expansion between the substrate and film. This heating due to the electromagnet and fluctuations in the temperature of the room and apparatus (from changing levels of sunlight) added noise and spurious signals

to the measurement. Unfortunately these noise and random signal levels were above those due to the cantilever movement caused by magnetostriction effects in the LAM films.

Because of the measurement difficulties with LAM films and apparatus location constraints (Lille, France), an uncommon magnetic field source, with a reversible and completely variable magnetic field, was constructed at UT using permanent magnets (NdFeB). It was designed to mimic the characteristics of the electromagnet at IEMN (bore size = 30 mm, uniformity of field, and maximum field strength). The advantages are: (1) a full hysteresis loop could be measured in about 30 seconds since there is no settling time, (2) a large switchable current supply is not required, and (3) the sample temperature is not perturbed due to the small measurement time and lack of heat from the coil of an electromagnet. In addition, the whole assembly can be enclosed in a small space reducing air currents and facilitating temperature stability. The magnet assembly was constructed from readily available components for a total cost in materials of about 500 USD.

4.2.2 Background

The type of magnet that was constructed was based on the vectorial addition of the magnetic fields from multiple permanent magnets. The idea was introduced by Halbach [29] after the development of high coercivity magnets that could withstand the demagnetizing fields from nearby magnets. Figure 4.3 shows two (related)

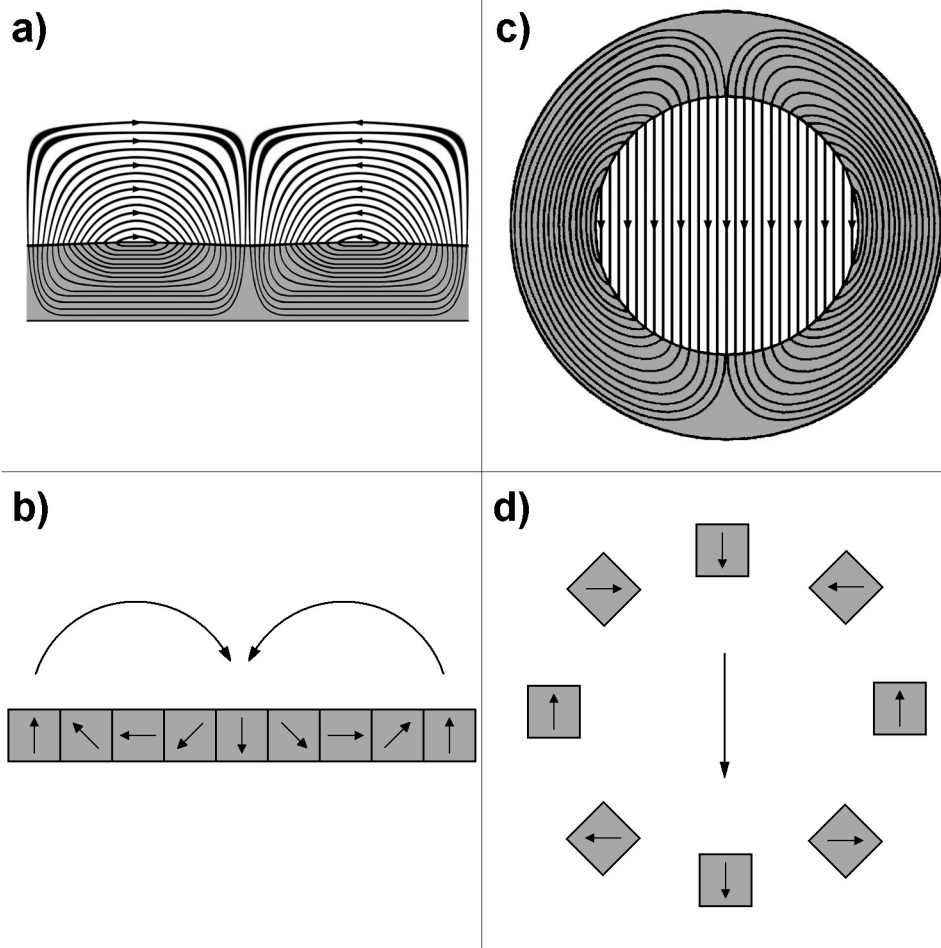


Figure 4.3 Schematic diagram of the magnetic configurations of permanent magnetic material shown schematically with flux lines. **a)** an ideal Halbach array. **b)** discrete approximation to the Halbach array. **c)** an ideal Halbach cylinder. **d)** discrete approximation to the Halbach cylinder.

configurations of permanent magnets that are named after K. Halbach. In both cases, there is the ideal monolithic magnetic material, magnetized with the proper orientation, and the approximation using discrete blocks of magnetic material. The first

configuration, Fig. 4.3a and b, is a linear periodic arrangement of blocks of magnetic material. Only one period is shown. It produces, in effect, a one-sided magnet. The other configuration, Fig. 4.3c and d, is called a Halbach cylinder and has a uniform field in the interior. It can be obtained by wrapping one period of a Halbach array into a cylinder. Wrapping more integer periods of the linear array into a cylinder would create a multipole interior field. Conversely, un-wrapping an ideal Halbach cylinder creates the ideal Halbach array with perfect cancellation of the fields on one side and complete reinforcement of the fields on the other.

The interior field strength, H , of a perfect Halbach cylinder is uniform, and depends upon the remnant field strength of the magnetic material M_r , and the inner and outer radii, r_i and r_o as given by

$$H = M_r \ln\left(\frac{r_o}{r_i}\right). \quad (4.7)$$

Equation (4.7) also shows that two cylinders may be of different sizes and yet have the same field strength inside. This leads to the possibility of constructing a variable magnetic field using two concentric Halbach cylinders that have identical interior field strengths. By rotating one cylinder with respect to the other, the fields in the interior will add (vectorially) creating a field that can be changed from zero to twice the field of each individual cylinder [30]. In fact, a campus company at Trinity College Dublin, Ireland, called Magnetic Solutions Ltd, at one time produced such a variable magnetic field source, though they no longer do so for safety reasons [31]. The extreme forces

encountered and the brittle nature of the high field strength, high coercivity magnetic material, created dangerous situations during assembly and operation. However, Halbach cylinders are used individually to create high field strengths for particle beam steering, spectroscopy, etc.

Another possibility for creating a variable magnetic field stems from the fact that, depending on which way a Halbach cylinder is wrapped from a linear array, the field will be either on the inside or the outside of the cylinder. If the array were created from individual segments of magnetic material, and then wrapped into a cylindrical geometry, the only difference between having the field inside or outside the cylinder would be that the magnetic field orientation of the individual segments were rotated $\pm 90^\circ$. Supposing the blocks were numbered consecutively, odd blocks would rotate $+90^\circ$ and even blocks would rotate -90° . Hence, by rotating individual segments in the proper direction, it is possible to vary the field strength continuously from zero to a maximum value. It is also worth noting that if all segments were rotated in the same direction, the summed field would not change strength but would rotate in phase with the segments. A magnetic assembly that uses the coordinated motion of the individual magnets to vary or rotate the magnetic field, has been dubbed a ‘Magic Mangle,’ [32] presumably due to the contorted mixing of magnetic fields from the individual magnets.

Figure 4.4 shows snapshots of the different magnet rotation positions for a magnetic mangle, composed of eight individual segments (individual permanent magnets). Starting from the maximum field configuration, 0° , (that which approximates

a Halbach cylinder), a rotation of 90° (recall neighboring segments rotate in opposite directions) brings about a configuration of minimum field strength. Theoretically, this is zero, but in practice it was a few tens of Oersted (2% of the maximum field strength) due to the fact that all the individual fields do not perfectly cancel. Rotating further to 180° corresponds to a field having the same strength as the original configuration but opposite in direction. Rotation to 270° is again a minimum field configuration.

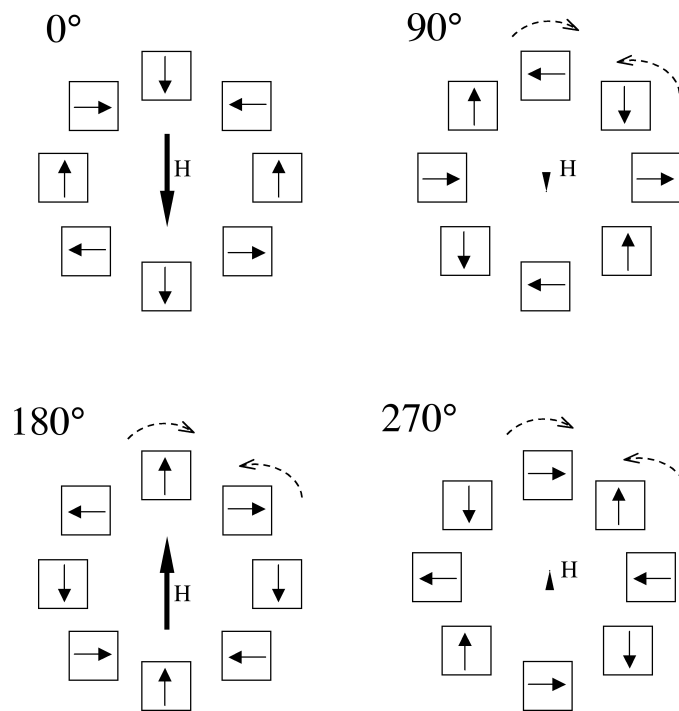


Figure 4.4 Schematic of the rotation of individual magnets for an N=8 magnetic angle.

This clever arrangement yields a magnetic field source that is reversible, fully variable, and whose strength is sinusoidally dependent on the angle of rotation. This fact was used in the calibration of the field and its measurement. Specifics of the magnet assembly follow in the next section.

4.2.3 Field Properties

The magnet assembly created at UT used eight individual rectangular magnet segments of NdFeB 25 mm x 25 mm x 75 mm, magnetized perpendicular to the long axis. The number eight was chosen as a compromise between uniformity and maximum field strength. The more individual magnets that are used, the more uniform the field, but the larger the minimum diameter circle that they fit circumferentially around and hence the smaller the field strength in the center. Equation (4.7) was used in the preliminary design phase by modeling the assembly as a Halbach cylinder with the same inner radius and cross sectional area of magnetic material as the collected segments. The final stages of design were verified with a 2-D magnetostatic modeling program from Ansoft, inc. called Maxwell 2-D. The simulations shown in Figs. 4.5 and 4.6 were found to correspond well to the actual device in terms of maximum field strength and field uniformity.

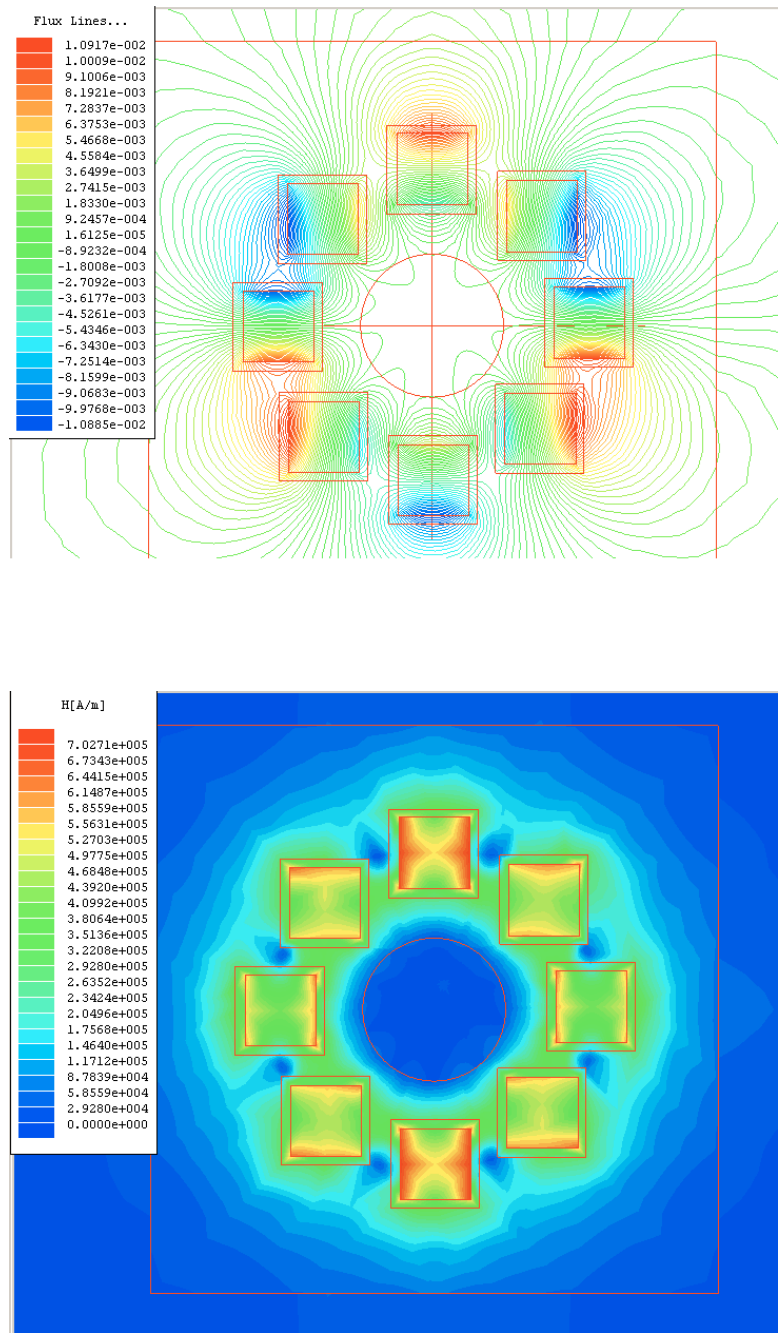


Figure 4.5 Simulation using Ansoft Maxwell 2-D, of an N=8 magnetic mangle for the minimum field configuration. Top: Flux lines, Bottom: field strength H (A/m).

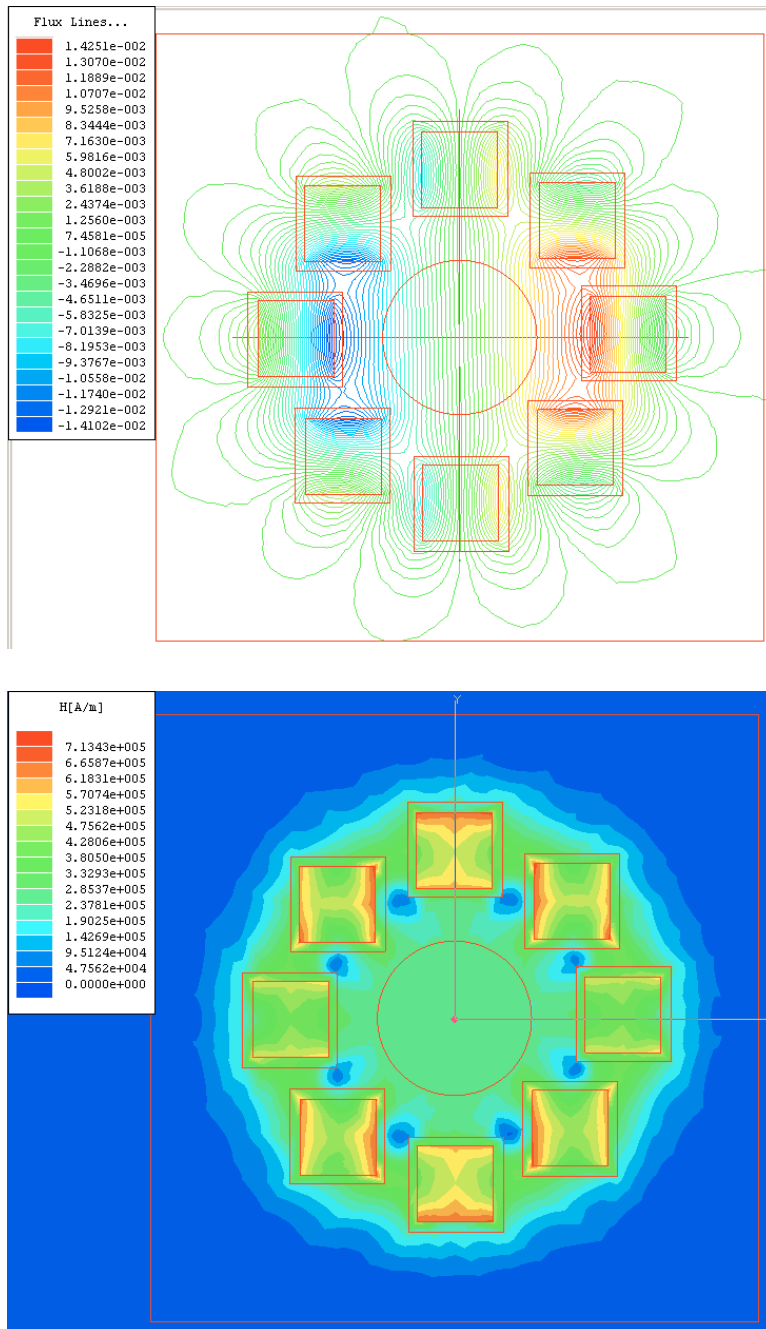


Figure 4.6 Simulation using Ansoft Maxwell 2-D, of an N=8 magnetic mangle for the maximum field configuration. Top: Flux lines, Bottom: field strength H (A/m).

As mentioned previously, the zero field configuration of the magnet assembly did not produce a zero strength field at the center. This was due to the imperfect cancellation of the magnetic fields from the individual magnets and resulted in a field strength of a few 10s of Oersted. Figure 4.7 shows the uniformity of the field strength along the axis of the assembly for a minimum field configuration. The uniformity of the field is on the order of 50 Oe over the center 20 mm on the axis of the magnet assembly. A property of the assembly is that the uniformity is only dependent on how

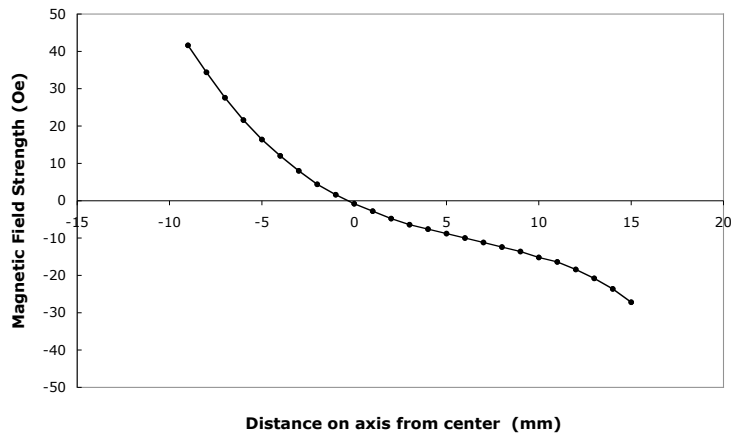


Figure 4.7 Hall probe measurement of the on-axis magnetic field for the minimum field configuration of the magnet assembly. 0 mm marks the center.

well the fields from the individual segments add and does not depend on the field strength. Thus, the uniformity at the maximum field of 2300 Oe was also about 50 Oe over 20 mm (2% of the maximum field strength).

The magnet assembly performed as designed and facilitated the measurement of magnetostriction of LAM films. One caveat however: due to the fact that “permanent” magnets are not permanent, the maximum field strength degraded to 2300 Oe, about 2/3 of the original maximum (3150 Oe) over the course of a year.

4.4 Optical Emission Spectroscopy

As discussed in Ch. 2, magnetic materials are sensitive to the state of oxidation of the magnetic atoms. Due to the fact that LAM samples must be exposed to air in the transfer to microanalysis machines or coated with an encapsulation layer that hinders the chemical composition analysis, the exact oxygen content in the nanoparticles or LAM films is difficult to quantify by using EDS or other microanalysis techniques. Thus, it was important to find an in situ oxygen diagnostic for the ablation and nanoparticle formation region.

Because a plasma is created during laser ablation and individual atoms are excited and emit characteristic wavelengths, optical spectroscopy can be used to determine the elements present. This is known in the literature as Laser Induced Breakdown Spectroscopy (LIBS), Laser Induced Plasma Spectroscopy (LIPS), or even more generally, Optical Emission Spectroscopy (OES), and these terms are often used interchangeably. It is a technique that is capable of determining trace elements at a level of parts per billion with proper statistics, calibration, and time gating [33]. Using this method to indicate the presence of atomic oxygen during ablation does not

distinguish the source of the oxygen, whether it be oxide in the bulk or on the surface of the microparticles, water or other oxygen containing molecules adsorbed on their surface, or oxygen impurities in the background gas. On the other hand, none of these sources of oxygen (especially as it is excited oxygen) are acceptable in the production of oxygen free nanoparticles.

Thus, a near-infrared spectrometer was used with the LAM apparatus in order to help diagnose and minimize sources of oxygen. The strongest spectral lines of oxygen occur at 777 nm and 845 nm, in the near infrared. A schematic diagram of the spectroscopic arrangement is shown in Fig 4.8. The spectrometer was a StellerNet, inc. EPP2000-NIR2 portable spectrometer with integrated holographic grating (1200 lines/mm), CCD detector (2048 pixels (14 μm x 200 μm)), and 12-bit A/D converter electronics. Data transfer was via a USB 2.0 connection to a desktop PC. The first-order spectrum was situated in the wavelength range from 600 to 1100 nm.

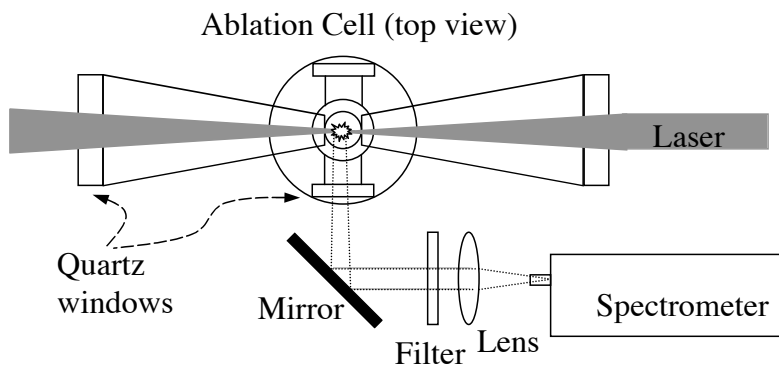


Figure 4.8 Emission Spectroscopy setup. Filter is removable Corning “sharp cut red” number 2-63 with a cutoff wavelength of 590 nm.

There were no filters inside the spectrometer, and so detection of the second order spectrum from 300 to 550 nm was also possible. The use of an external filter, a Corning 2-63 “sharp cut red” filter, with a cutoff wavelength of 590 nm served to block the second order. A transmission spectrum of the filter and the quartz viewing window on the ablation cell are shown in Fig. 4.9. Calibration of the spectrometer was done using a high-pressure mercury-argon lamp, with and without the red cut filter. A short (2 cm) focal length lens imaged the ablation plasma onto the detector entrance slit directly or onto an optical fiber that led to the spectrometer.

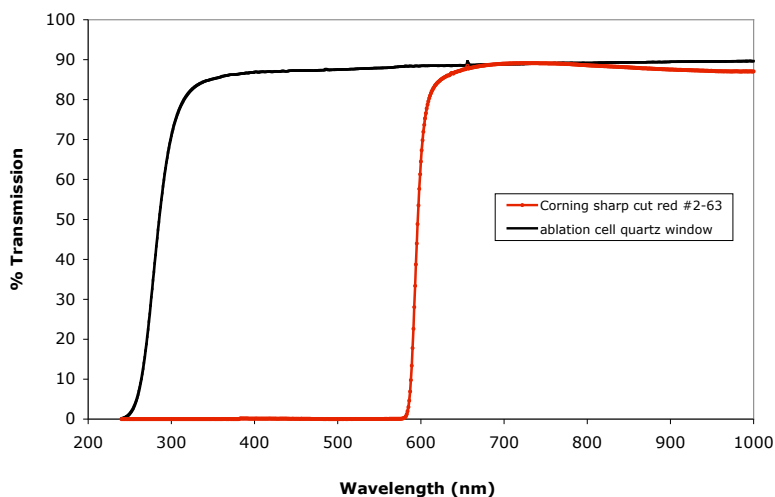


Figure 4.9 UV-VIS transmission spectra of the sharp cut red filter and the quartz viewing window of the ablation cell.

A sample emission spectrum from a helium low-pressure discharge lamp is shown in Fig. 4.10. The filter was in place, so only the first order wavelengths (600 to 1050 nm) are displayed. This type of discharge lamp is not sold specifically for wavelength calibration as is the high-pressure mercury-argon lamp, but for educational use in atomic spectroscopy. Thus, the helium in the lamp is not ultra-high purity helium and significant peaks due to oxygen and hydrogen can be seen in the spectrum, indicating water and oxygen contamination in the helium.

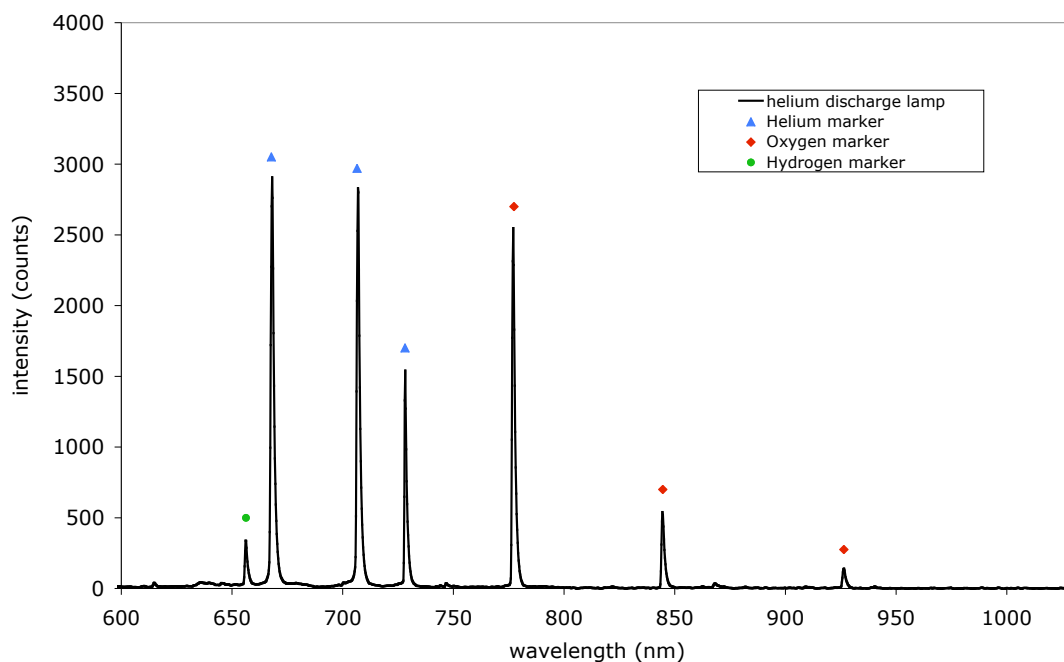


Figure 4.10 Spectrum of a helium low pressure discharge lamp with peaks identified. The hydrogen and oxygen peaks are due to water and oxygen contamination in the helium.

The aforementioned techniques and apparatus in this chapter provided the means for analyzing films on cantilevers with respect to magnetostriction and elastic modulus. In addition, optical emission spectroscopy provided a way to determine the presence of oxygen in the ablation plasma. The following chapter, Data and Analysis, provides representative data obtained from the films deposited by supersonic impaction of nanoparticles made from LAM of Terfenol-D, and from spectroscopic observation of the laser ablation region in the LAM process.

5

Data and Analysis

The goal of this research was to use the LAM process and subsequent supersonic nanoparticle impactation described in Ch. 3 for deposition of magnetostrictive actuator material. Thus, nanoparticles created from laser ablation of an aerosol of Terfenol-D microparticles in the LAM process were supersonically impacted onto various substrate materials (silicon, glass, and plastic) in the form of cantilevers. These samples were then analyzed using the methods and techniques described in Ch. 4. This chapter contains a representative set of the data and analysis of those samples, including physical film properties, microstructure and chemical analysis, and magnetic properties. Additionally, spectroscopic data of the ablation plasma inherent to the LAM process is presented.

5.1 Film Properties

5.1.1 Physical Appearance and Geometry

The films made by the supersonic impaction of nanoparticles using the LAM method are typically dark grey to black in color. This is due to the oxidation and, in a large part, the texture of the surface as evidenced by previous work with silver and copper nanoparticles that had a similar appearance. Figure 5.1 shows a photograph of one such Terfenol-D film, deposited on a glass substrate and mounted on the fixture used to measure tip deflection versus magnetic field or temperature. The ruler in the photo was used for image pixel calibration to determine the film and substrate length and width. The precision of this method of measuring distance was on the order of 0.1 mm with a 3 megapixel camera in macro mode.

In order to determine the average height of the film, profiles were taken using a Dektak profilometer. An example of this type of profile is shown in Fig. 5.2. In general, profilometry showed that the films were neither smooth, nor flat, with typical surface variations on the order of 0.5 μm . The film thickness is dependent on the spacing of the individual lines that make up the film and the profile of the lines themselves. It is also largely dependent on the feeding of the microparticles into the ablation region. Variations in feed density show up as large-scale changes in the height of the film. These variations are due to the amount of powder in the feeder, the particle size distribution of the powder, and what frequency and how much vibration is used to fluidize the particle bed in the feeder, etc. The decrease in film height over time due to

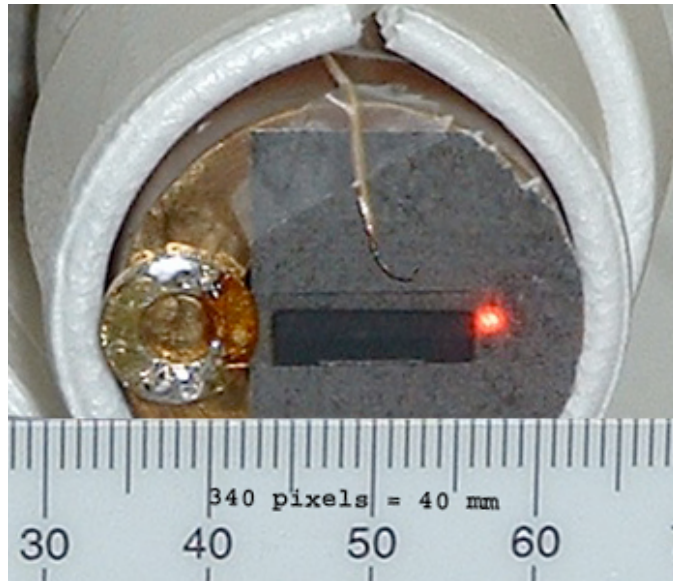


Figure 5.1 Photograph of a LAM film on a glass substrate cantilever mounted on the fixture for determining tip deflection vs. magnetic field or temperature. Part of the styrofoam insulation, the thermocouple, and the laser spot are visible. The ruler is used for calibrating image pixels to determine the cantilever and film dimensions.

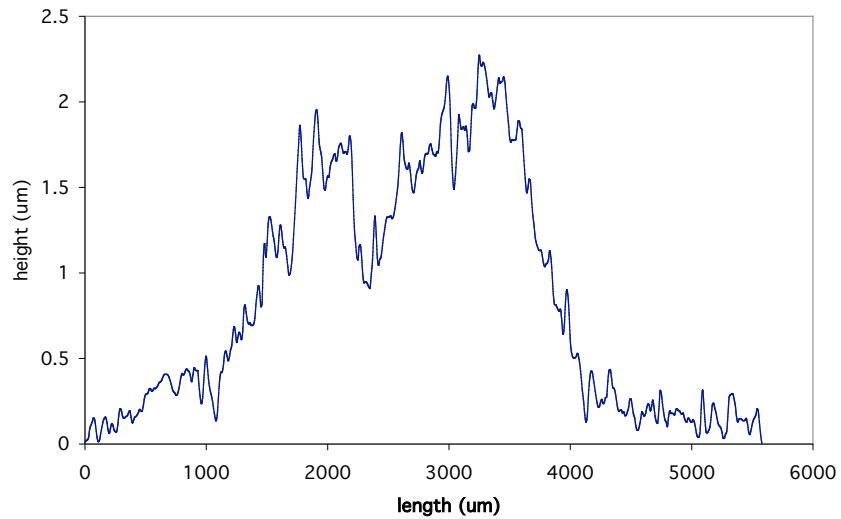


Figure 5.2 Profilometry of a LAM of Terfenol-D film taken across the writing direction.

diminishing powder in the feeder can be seen in Fig. 5.2 (right to left). For this film, the average height over the entire deposited width is $0.85\ \mu\text{m}$, with a peak height of $2.3\ \mu\text{m}$. The average film height was used in all calculations requiring film thickness.

5.1.2 Elastic Modulus

The tip deflection of a bi-layer cantilever, due to magnetostriction of one of the layers, depends upon the magnetostriction value, the geometry of the film and substrate, and their elastic moduli (cf. Eq. (4.1)). From previous work, films made from supersonically impacting silver nanoparticles under similar conditions are porous and have densities on the order of 60–70 % of the bulk value of silver. This reduces the elastic modulus of the film and hence it is not appropriate to use the value of bulk Terfenol-D in the calculation of magnetostriction. The density and elastic modulus are related empirically through Eq. (4.3), but a more direct measure of the modulus can be obtained through the bending and tip deflection of a cantilever due to the different coefficients of thermal expansion (which do not depend on density) of the film and substrate.

The tip deflection vs. temperature of one sample (that pictured in the photograph of Fig. 5.1) of a LAM of Terfenol-D film deposited on a glass substrate is shown in Fig. 5.3. Due to the imperfect insulation of the oven, there is a small hysteresis loop in the data due to the fact that the thermocouple and cantilever have different rates of heat gain and loss. Two consecutive loops are shown in Fig. 5.3.

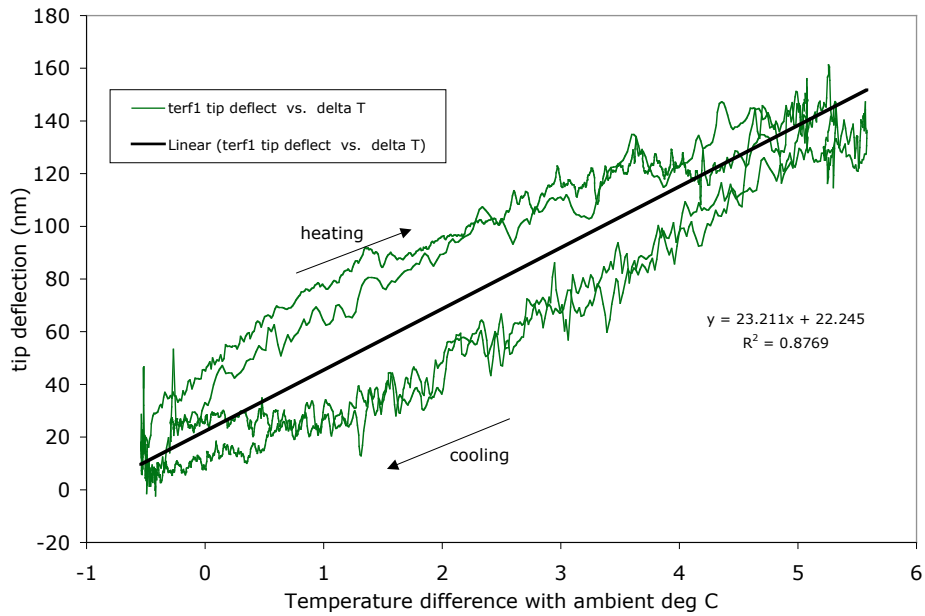


Figure 5.3 Temperature cycle loops of LAM of Terfenol-D deposited on a glass cantilever to obtain modulus and density/porosity.

The average slope of the two loops is taken from a straight line fit of the entire data set. For validation, just the individual cooling curves are shown and fitted in Fig. 5.4. Since the (average) slopes of the two fitting methods are nearly identical and the hysteresis loop is symmetric, it can be inferred that the small magnetic field due to the current in the heater coil of the oven (present only while increasing the temperature) did not impact the measurement of this sample. This was in fact the case for all samples measured.

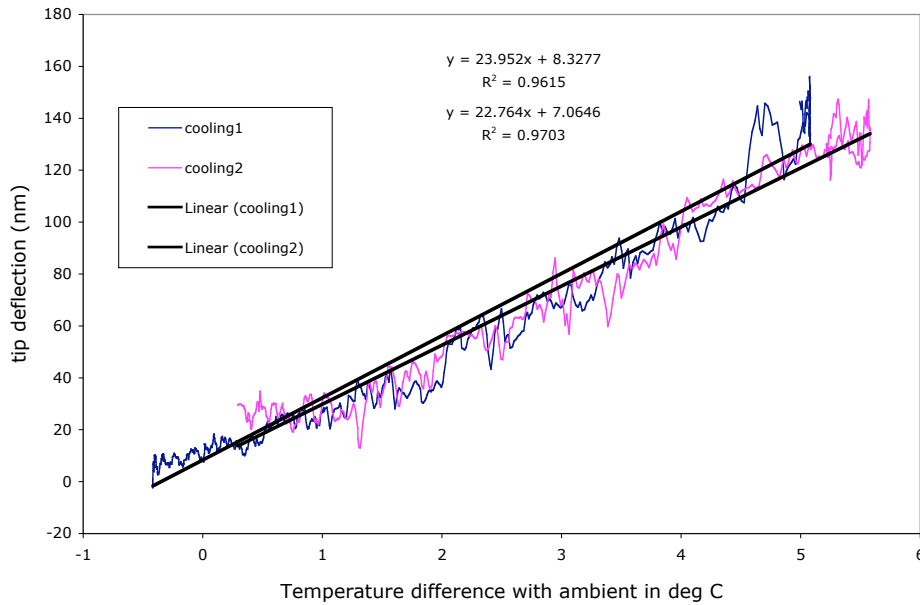


Figure 5.4 Cooling curves only of Fig. 5.3 of LAM of Terfenol-D, deposited on a glass cantilever to obtain modulus and density/porosity.

From the slope of the linearly fitted deflection vs. temperature curve, this particular sample had a tip deflection of 23 nm/°C. Equation 4.2 relates the geometry and elastic modulus of the film and substrate for a bi-layer cantilever to the tip deflection due to a change in temperature. Using this equation with the film geometry and the above value for temperature dependent tip deflection leads to an elastic modulus of the LAM film of 14 GPa. Terfenol-D, both in bulk and in film form, has an elastic modulus that is dependent on the crystalline and stress state the material is in and hence varies over a wide range of values. Common values reported for unstressed bulk

Terfenol-D range from 25 to 50 GPa. Powder composites, which are casts of Terfenol-D powder mixed with a polymer binder and have densities on the order of 75 to 85 % of bulk Terfenol-D, have elastic modulus values ranging from 16 to 25 GPa [34]. The elastic modulus of LAM films is consistent with values for particle composites, though in the LAM films, the non-Terfenol-D component is low pressure helium (for closed porosity) from the deposition chamber or atmospheric gas (for open porosity) as opposed to an organic binder. This causes a further reduction in the elastic modulus for a given density of active material compared to composites.

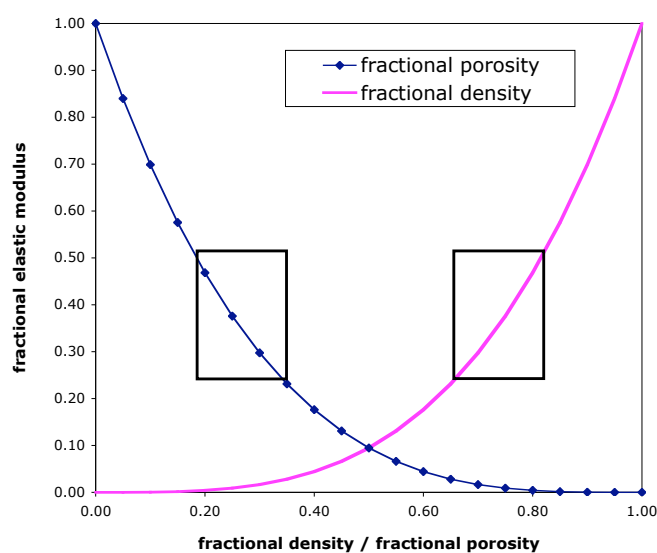


Figure 5.5 Plot of elastic modulus dependence on porosity (density) in terms of the percent of the bulk values, after Eq. (4.4). Square boxes indicate the range of calculated values for LAM films.

Equation (4.4), empirically relates elastic modulus and porosity (or density) for powder compacts of various iron compounds. Using this equation with the values 25 and 50 GPa as the bulk elastic modulus of Terfenol-D, and the above value of 14 GPa for LAM films, results in a porosity of 20 to 35% , or conversely, a density between 80 and 65% of the bulk value of Terfenol-D. This is consistent with previous data collected for silver under similar deposition conditions. Figure 5.5 shows a plot of the dependence of elastic modulus on porosity (or density) from Eq. (4.4), annotated with the range of calculated values for LAM films.

From Eq. (4.3), it is clear that the elastic modulus, and hence porosity, plays a significant role in the ability of the deposited film to be used as an actuator. For example, a reduction of the elastic modulus by half reduces the tip deflection of a cantilever by half as well. However, the LAM film porosity and elastic modulus is not overly different from that of current powder composites and hence should be capable of similar strains. This implies that the reduction in elastic modulus due to the porosity of the film does not explain the weak actuation behavior of the LAM films. Examples of tip deflection vs. magnetic field are presented in section 5.2.

5.1.3 Microstructure and Chemical Composition

As was previously described in Ch. 3, the nanoparticles generated by feeding microparticles of Terfenol-D in the LAM system are typically between 3 and 20 nm in diameter with a maximum in the size distribution occurring below 10 nm. Figure 5.6 repeats the bottom image of Fig. 3.3 alongside a copper nanoparticle also generated by the LAM process. The copper particle is large enough to show an amorphous surface oxide layer and lattice fringes due to the crystalline structure of the core. It is clear that the nanoparticle from LAM of Terfenol-D is amorphous in comparison with the copper nanoparticle and the amorphous carbon background of the image.

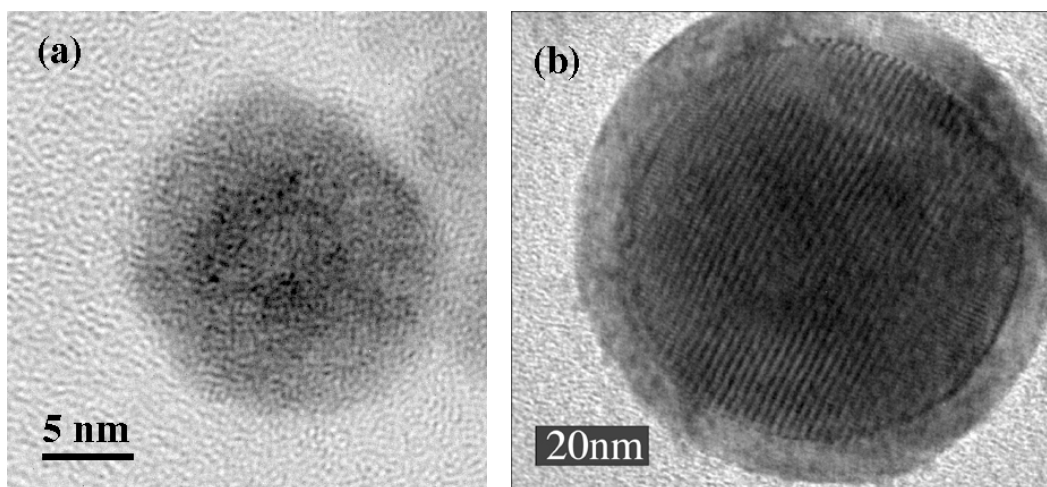


Figure 5.6 (a) Reproduction from Fig. 3.3b. HRTEM of a nanoparticle after ablation of Terfenol-D microparticles showing similar atomic order to the background amorphous carbon support film. Used with permission from James Ma. **(b)** Large copper nanoparticle made using the LAM method showing atomic lattice planes and an amorphous oxide shell. Used with permission from Gokul Malyavanatham.

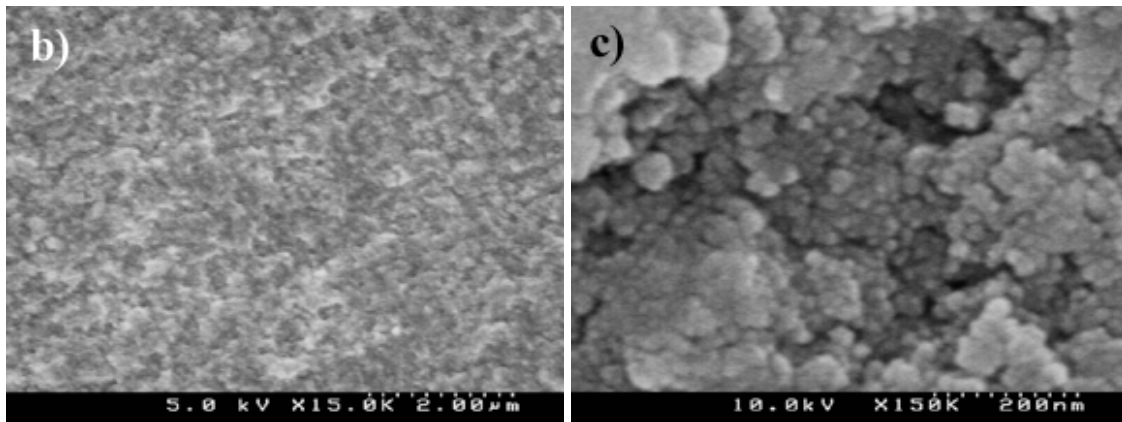
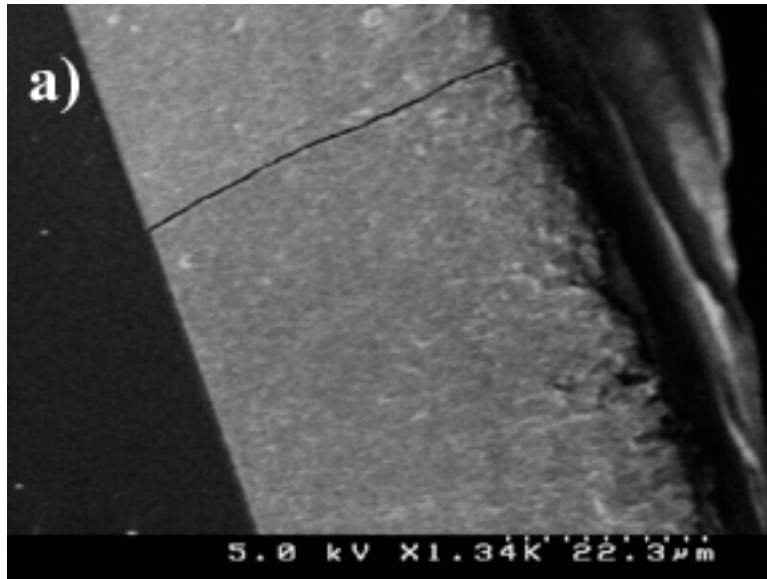


Figure 5.7 (a) Low magnification cross-section SEM image of film from LAM of terfenol-D. The silicon substrate is on the left side of the image and a crack can be seen running through the entire film. (b) Medium magnification of the center region of (a). (c) Highest magnification showing the granular nature of the film.

Cross-sectional SEM micrographs of a representative film are pictured at different magnifications in Fig. 5.7. The micrograph at the highest magnification of the interior structure (Fig. 5.7c) indicates the particulate nature of the film and the fact that

the film fractures at the interface between particles (or groups of particles) and not through a particle.

To verify the amorphous nature of the deposit, x-ray diffraction (XRD) data was taken on certain films. Figure 5.8 shows such XRD data comparing the starting Terfenol-D microparticles with the LAM deposited film. There appears to be no crystalline nature to the film and the single peak at 2-Theta = 69° is due to the single crystal silicon substrate.

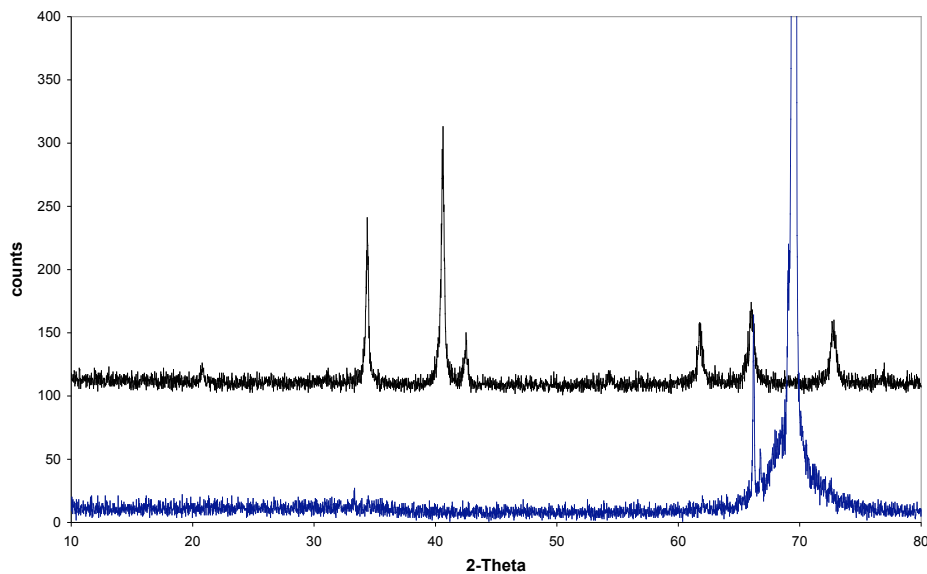


Figure 5.8 X-ray diffraction data of a LAM film (lower/blue curve) and starting Terfenol-D microparticles (upper/black curve). Other than the large peak at 2-Theta = 69° which is the silicon substrate, the lack of peaks shows the amorphous nature of the deposited film. Used with permission from James Ma.

Table 5.1 EDS measurements of Microparticles and LAM deposited Terfenol-D. All results are in atomic percent, i.e., the sum of all elements displayed is equal to 100. Data used with permission from James Ma.

Feedstock Microparticles

	O	Fe	Tb	Dy
Spectrum 1	52.90	32.70	4.60	9.80
Spectrum 2	50.12	33.14	4.77	11.97
Spectrum 3	47.60	34.78	5.52	12.09
Mean	50.21	33.54	4.96	11.29
Std. Dev	2.65	1.10	0.49	1.29

LAM film (measured August 2004)

	O	Fe	Tb	Dy
Spectrum 1	57.75	31.50	4.63	6.13
Spectrum 2	60.16	29.98	3.08	6.78
Spectrum 3	62.71	27.33	3.15	6.81
Spectrum 4	61.69	29.05	3.30	5.96
Mean	60.58	29.47	3.54	6.42
Std. Dev	2.16	1.75	0.73	0.44

LAM film (re-measured in February 2005)

	O	Fe	Tb	Dy
Spectrum 1	67.81	23.00	2.34	6.85
Spectrum 2	67.96	22.96	2.36	6.71
Spectrum 3	68.32	22.83	2.41	6.43
Spectrum 4	68.39	22.44	2.55	6.62
Mean	68.12	22.81	2.42	6.65
Std. Dev	0.28	0.25	0.09	0.18

Composition of the films was also investigated using Energy Dispersive Spectroscopy (EDS) in the SEM. The nature of the measurement is the spectroscopy of x-rays emitted from the sample due to electron bombardment. Because of this, low energy x-rays from the light element oxygen are easily blocked by the detector window,

neighboring heavy elements (like iron and the rare earths) and in particular any protective overcoatings. Hence quantitative oxidation analysis using EDS is poor, though it does give qualitative information. Composition data of a LAM film without a protective coating of gold are given in Table 5.1. The data is graphed in Fig. 5.9 after being re-normalized to iron = 2 for convenience in comparing the data to the standard chemical composition of Terfenol-D ($Tb_{0.3}Dy_{0.7}Fe_{1.92}$), which is a member of the RFe_2 (R = rare earth) system of magnetostrictive alloys.

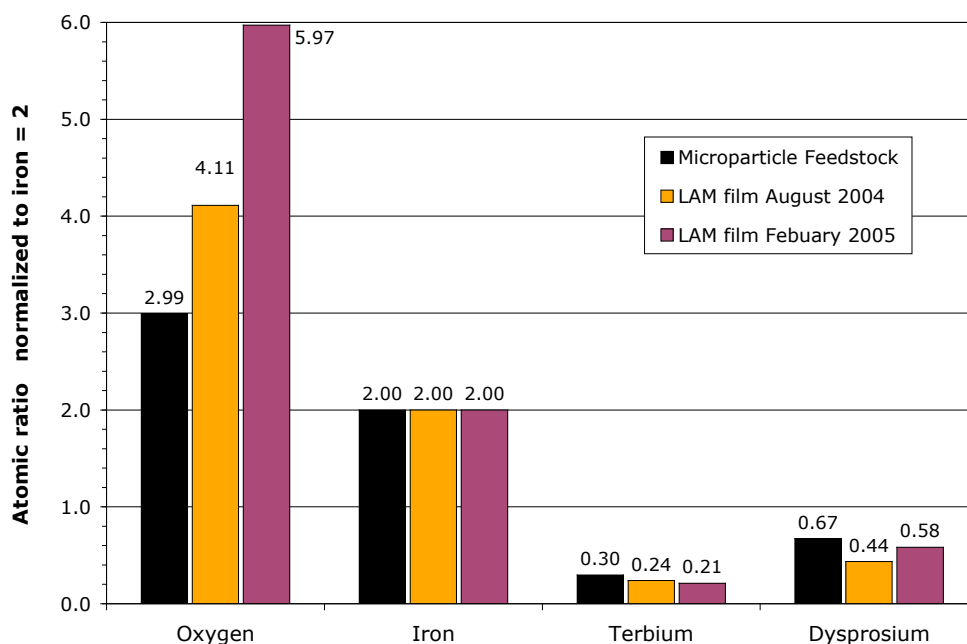


Figure 5.9 Chemical composition of microparticle feedstock (black) and LAM deposited Terfenol-D as made (yellow), and after 5 months (purple). Data from Table 5.1 normalized to iron = 2 for comparison with the nominal chemical composition values ($Tb_{0.3}Dy_{0.7}Fe_2$)

This data shows that over a period of 5 months the film was further oxidized indicating that at least part of the film was not initially oxidized. The atomic ratios of Tb/Dy and (Tb + Dy)/Fe show the correct trends, though there is an excess of iron. It is suggested that in the LAM process the composition of the feedstock material is preserved in the nanoparticles that are formed behind the shockwave, but not necessarily for the nanoparticles formed from the surface material evaporated due to the initial absorption of the laser. As this is an evaporative process it can cause elemental segregation due to the different boiling points of the elements. TEM-EDS analysis of small groups of nanoparticles indicates that all three elements (Tb, Dy, and Fe) from the microparticle feedstock are present, though without quantitative information.

5.1.4 Magnetization

The magnetization hysteresis loops were taken using a SQUID magnetometer. The saturation magnetization for bulk Terfenol-D is 86 emu/g calculated from the accepted value of 1.0 Tesla and its mass density. Microparticles purchased from Etrema, inc. having a size range from 0 to 300 μm had a saturation magnetization of 70 emu/g after exposure to air. Typical values for LAM films were 5–10 emu/g after exposure to air. A few test deposits in the form of lines with protective gold coatings had values as high as 30 emu/g with coercivities of 20 Oe. Thin films of $\text{Tb}_{0.3}\text{Dy}_{0.7}\text{Fe}_2$ are reported to have a saturation magnetization between 20 and 50 emu/g depending on composition and crystal structure, with amorphous films having the lower value [35].

Powder composites have values between 60 and 75 emu/g. An example of a typical hysteresis loop measured for LAM films is plotted in Fig. 5.10. This particular plot shows data for the film for which composition data is give in Table 5.1. Of note is the decrease in saturation magnetization from 5.5 to 5.2 emu/g after 5 months at ambient conditions. The coercive field remained unchanged at 70 Oe.

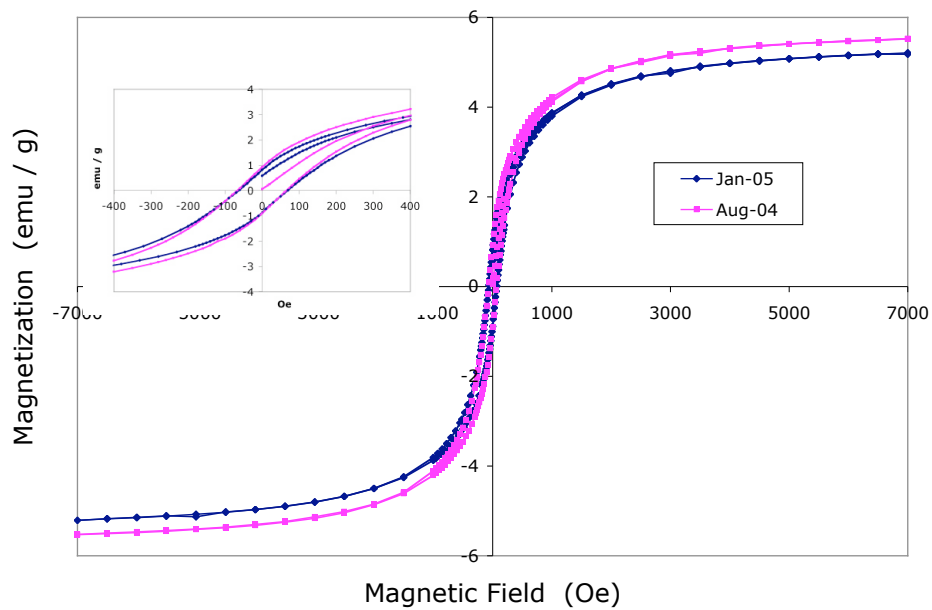


Figure 5.10 Magnetization curves of a LAM deposited TbDyFe film. The value of saturation magnetization of bulk Terfenol-D is 86 emu/g. Used with permission from James Ma.

5.2 Magnetostriction

The focus and main objective of this research was the utilization of the LAM method with Terfenol-D for the generation of nanoparticles and subsequent supersonic impaction to deposit films of a magnetostrictive material. However, due to the weak

magnetostrictive response of the LAM films, cantilevers with films made by two other methods were used to verify, not only the measurement apparatus and techniques of Ch. 4, but also the starting Terfenol-D material and laser ablation process as well. Film data, including calculated magnetostriction, are presented for comparison in Table 5.2 from samples of the three different deposition methods.

Table 5.2 Collected data of four magnetostrictive RFe₂ type films deposited on cantilevers using three different deposition methods.

	LAM		PLD	TbFe ₂
Substrate -	glass	Mylar	silicon	silicon
- thickness, (μm)	160	150	125	150
- elastic modulus, (GPa)	70	5	110	110
Film -				
- length, (mm)	12.6	12	10.7	10
- thickness (μm)	1	1 ^b	0.5	1.5
- elastic modulus (GPa)	14 ^a	14 ^b	30 ^b	30 ^b
- saturation magnetization (emu/g) *	6	^c	16	10
- coercivity (Oe)	70	^c	30	160
- tip deflection $d_{ }$ @ 2 kOe (μm)	0.09	0.4	0.80	2.00
- magnetostriction @ 2 kOe (ppm) ^a	16	9	310	490
- magnetoelastic coupling coeff. (MPa) ^a	0.13	.08	5.4	8.5

^a calculated value, ^b assumed value, ^c not measured, * mass (g) was calculated from volume

The two sample types other than the LAM made samples were, 1) a TbFe₂ film made in France by RF Sputtering a composite target of iron and terbium, and 2) a PLD film made in Austin by Pulsed Laser Deposition of a commercially purchased target of Terfenol-D (Tb_{0.3}Dy_{0.7}Fe_{1.92}) under UHV (ultra high vacuum) conditions, using the same KrF laser as in LAM. The target material used for the PLD film was identical to

the Terfenol-D that was ground into powder to obtain the microparticles used in the deposition of LAM films.

The TbFe₂ film sample had been well characterized by the team at IEMN (France), and so was used as a verification of the measurement setup at UT (USA). The PLD film provided another independent verification of the measurement setup, but more importantly, provided a means of depositing a film from the same starting Terfenol-D as was used in the LAM films, and that used a (similar) laser ablation mechanism, but had important process differences. These differences were the fact that the surface of the target could be cleaned in situ by the laser before deposition, the deposition occurred in oxygen free ultra-high vacuum (10⁻⁹ Torr), and the deposited films were fully dense. The author wishes to credit James Ma with this ingenious idea and its implementation.

Deflection curves due to a magnetic field applied parallel to the cantilevers are shown in Figure 5.11 for four samples: the two described above and two LAM samples. The LAM films are the one shown in Fig 5.1 deposited on a glass substrate and one deposited on Mylar (a trade name plastic) under similar conditions. Use of Mylar served to make the magnetostriction effect more visible due to its low elastic modulus. Of note is that none of the films presented here had protective coatings.

The tip deflection curves are not completely comparable among themselves even though the cantilevers were all about the same length, as the magnitude of the deflection depends on film thickness and other sample properties that differed. However, it is

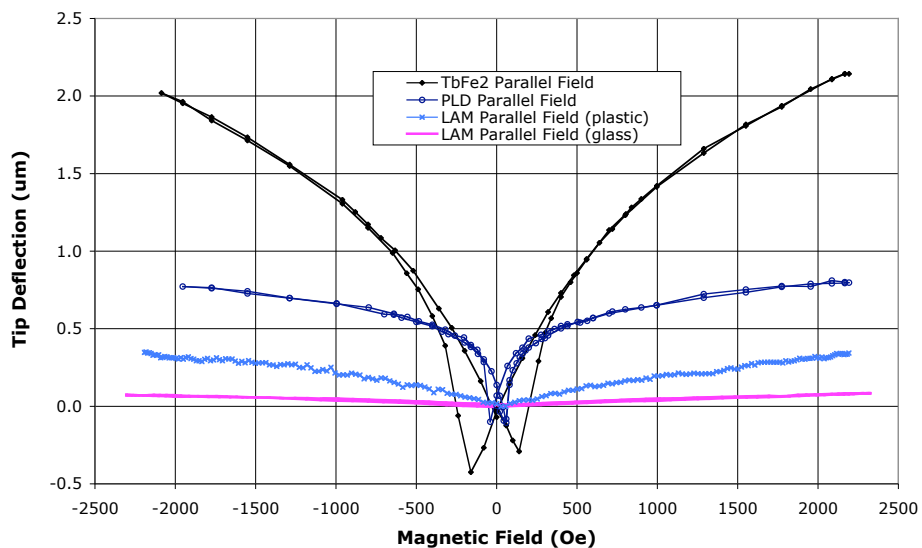


Figure 5.11 Chart showing tip deflections for 10 mm long cantilevers having films made with different processes: LAM deposited nanoparticles, PLD deposited film, and a conventional sputtered TbFe₂ film made in France.

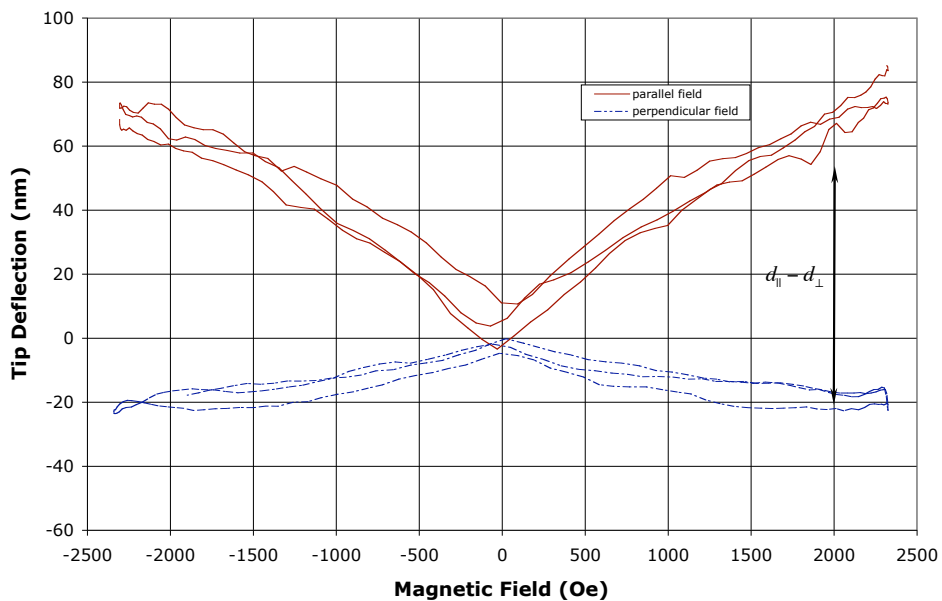


Figure 5.12 Plot of tip deflection vs. magnetic field for a LAM film on glass showing both parallel and perpendicular field curves. The quantity ($d_{||} - d_{\perp}$) used in the calculation of magnetostriction is shown on the right.

possible to see different behaviors of the films by looking at Fig. 5.11. The difference in coercivities is visible between the TbFe₂ film and the others. The PLD film saturates quickly, whereas the TbFe₂ and the LAM films do not show signs of saturation even though the LAM films had similar magnetization hysteresis curves to the PLD sample, the corner to saturation occurring around 1000 Oe (cf Fig 5.10).

Figure 5.12 shows a magnified view of the same magnetostriction curve for the LAM film on glass in Fig. 5.11, but for both parallel and perpendicular applied fields. The symmetry between the two curves shows how magnetically isotropic the film is and the difference between the tip deflection measurements ($d_{\parallel} - d_{\perp}$) is used in the calculation of magnetostriction. In this case there is a slight favoring of the width (perpendicular) dimension of the cantilever as an easy axis, as the tip deflection when the magnetic field was perpendicular to the cantilever was smaller. This implies more magnetic moments were already aligned in that direction reducing the number of moments being reoriented and causing elastic deformation. Additionally, the apparent lack of saturation in the tip deflection curves may be due to a perpendicular (i.e., normal to the film plane) magnetic anisotropy, that can arise from compressive stress in the film [36].

Using the elastic modulus data from the temperature dependence of the tip deflection, the LAM film on glass had a magnetostriction value of 16 ppm (at 2000 Oe). The magnetostriction of the PLD and TbFe₂ films using the same calculation method were 310 and 490 ppm (at 2000 Oe) respectively. The magnetostriction and the

magnetoelastic coupling coefficient, a measure of the film's ability to generate strain that is not calculated using the elastic modulus of the film, are presented in Table 5.2.

Comparison of the magnetoelastic coupling coefficients of Table 5.2, shows that the LAM film on glass had a value 1/40th that of the PLD film. That is to say, given equal film and cantilever geometries, the tip deflection due to the LAM film would be 1/40th of that due to the PLD film. Measurement of the elastic modulus shows that the LAM films have a modulus that is about half the expected value of Terfenol-D. The effect of modulus is significant, i.e., halving the modulus halves the tip deflection, but this value cannot entirely explain the weak deflection. It is likely that there was more oxidation of the LAM films compared to the others due to the fact that they were porous, though experiments using an in situ deposition of a protective gold layer did not improve the actuation. The low magnetostriction value for the LAM film deposited on Mylar may be due to the relatively high permeability of Mylar with respect to oxygen and water vapor. The bottom surface of the film in contact with the Mylar would be exposed to oxygen as well as the top surface. Hence it can be assumed that the nanoparticles themselves that are impacted into a film are at least, but most likely only, partially oxidized. This idea is supported by the fact that the PLD film was deposited in ultra high vacuum and had similar magnetostriction to the TbFe₂ film and the saturation magnetization of the LAM film decreased over time.

Spectroscopic observation of the ablation plasma is presented in the next section. This technique provided information on the environment that the nanoparticles formed in, and in particular, the presence of oxygen in that environment.

5.3 Ablation Spectra

Laser ablation in general creates a plasma due to absorption of the intense laser energy. As the plasma cools, the atoms emit light characteristic of the particular element. This provides a convenient method for the detection of oxygen in the ablation region of the LAM process where the nanoparticles are formed before being supersonically impacted into a film. Hence, the light from the ablation region was collected and directed to a spectrometer where individual elements could be distinguished by identifying the spectral peaks at their characteristic wavelengths.

As was described in Ch. 4, the spectrometer had no internal filter to separate the orders. Hence, simply collecting the light of the microparticle ablation plasma results in the upper spectra (green curve) of Fig. 5.13, a combination of second order light from 300 to 550 nm and first order light from 600 to 1100 nm. Iron, dysprosium and terbium have a large number of spectral lines though almost all lie in the visible wavelengths between 300 and 650 nm as opposed to the red and near-infrared above 650 nm. The strongest peaks in the spectra are due to the iron lines clustered around 490 nm and consequently the plasma appears greenish blue.

The use of a long-wavelength pass filter having a cutoff wavelength of 590 nm resulted in the second order wavelengths (300 to 550 nm), and consequently most of the emitted light, being rejected as shown by the lower emission spectrum (blue curve) of Fig. 5.13. This is advantageous as the strongest peaks of oxygen are the neutral atomic lines located around 777 nm and 845 nm, and hence these lines were well separated from the brightest and most cluttered part (from 300 to 650 nm) of the ablation spectrum and were easily identified.

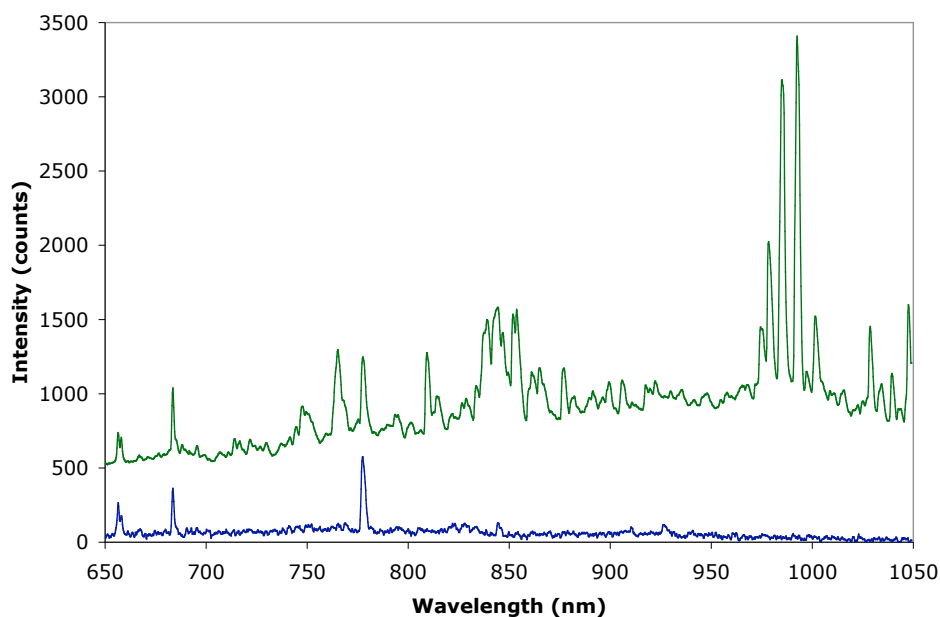


Figure 5.13 Example of emission spectra from laser ablation of Terfenol-D microparticles. Upper curve (green) spectrum without the Corning 2-63 sharp cut red filter – a long-wavelength pass filter (shifted for clarity). Lower (blue) spectrum with the filter.

Wavelengths from 650 to 850 nm of the first order-spectrum (lower/blue curve of Fig. 5.13) are re-plotted in Fig. 5.14 with the peaks identified. It is immediately clear that there is a strong oxygen presence in the plasma as evidenced by the peaks at 777 nm and 845 nm. The 777 line is in fact a triplet which causes the broad peak width, and the peak at 845 can be seen to be two closely spaced peaks at 844 and 846 nm. There is a hydrogen peak at 656 nm indicating the presence of water as one possible source of oxygen. The other peaks are from dysprosium at 658, 683, and 685 nm.

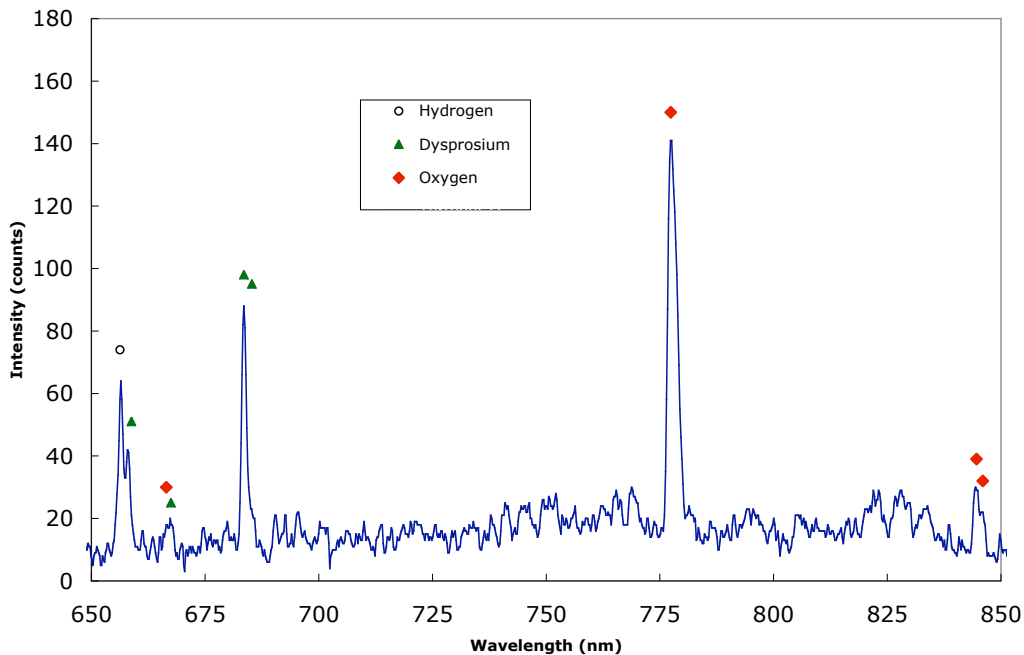


Figure 5.14 Excerpt of emission spectrum from laser ablation of Terfenol-D microparticles with filter. The peaks are identified with the emitting atom. The oxygen peak at 777 is actually a triplet, hence the broad linewidth.

It is interesting to note that there are no clear peaks due to excitation of the helium carrier gas at 707 or 728 nm as in the spectrum of the low-pressure discharge lamp of helium shown in Ch. 4. This is due to the fact that the breakdown mechanism of the microparticle aerosol of metallic particles due to the KrF laser is the absorption of the laser energy at the surface of the particles. The gas itself does not break down and the laser would pass through the focal volume without incident unless there were particles there to absorb the light. This is due to the fact that the laser is not focused to an energy density high enough to break down the pure background gas. Hence the emitted light of the ablation plasma is from the atoms of the ablated particle and not the background carrier gas, helium in this case. It must be true that some gas atoms are excited through collisions with the microparticle atoms and emit light, but these are a relatively tiny number compared with the number of atoms coming from the solid microparticle.

In order to further verify this view of the process, the laser was focused onto a solid plate of Terfenol-D and the spectra recorded both in air and in 99.99% pure helium at atmospheric pressure. The plate of Terfenol-D was from the same material that was ground into microparticles for the LAM films and used in the deposition of the PLD film analyzed in section 5.2. The advantage of a solid target over microparticles was that almost all of the energy of the laser pulse was absorbed and much of the material was ejected normal or nearly normal to the target surface. This should have increase the number of excited background gas atoms due to the larger amount of energy coupled to

the surrounding gas. Again, no helium peaks were visible for the case of ablation in helium, but a small from atomic nitrogen was visible in the ablation carried out in atmosphere as shown in Fig.5.15. However, the oxygen signal far outweighed that from nitrogen, and hence it can be concluded that the surface oxygen was responsible for the signal as opposed to excitation of the oxygen gas or water vapor in the atmosphere. This is particularly true when the background gas is high purity helium. The large peak widths of Fig 5.15 are due to collisional broadening from the high density of the ablated atoms coming from the solid target.

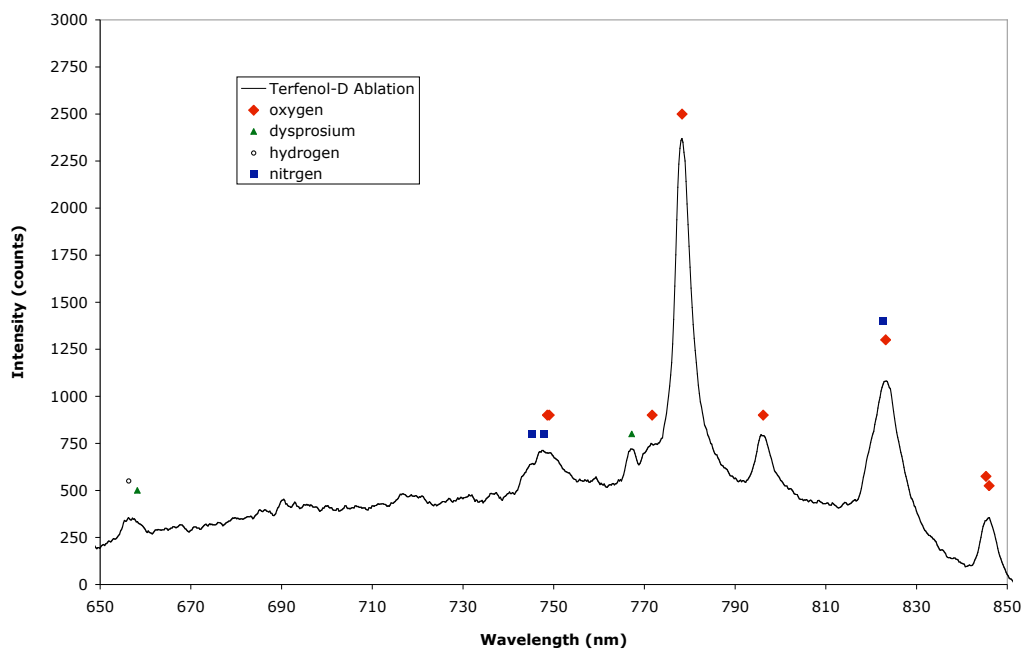


Figure 5.15 Spectrum of laser ablation of a solid plate of Terfenol-D in air.

While it was not possible to see the oxygen content of the background gas in real time from the ablation spectra, it was possible to investigate oxidation of a surface over time using laser ablation and spectroscopy. Another property of a solid target as opposed to microparticles is that the surface can be cleaned in situ by the laser. This is an advantage for deposition techniques like sputtering and PLD, where the first few moments of deposition can be blocked from reaching the substrate until a clean target surface is achieved. This is particularly useful after the vacuum system has been opened or a new target installed. In addition, because the KrF laser is a pulsed laser, ablation happens in discrete increments and so a small semi-consistent amount of material is removed at each laser pulse. Thus it is possible to look at the spectra of each pulse (or group of closely spaced pulses to increase the signal level) over time and gather qualitative information about the change in the target surface with time.

This experiment was conducted using the same plate of Terfenol-D that was used to make the feedstock powder for LAM films. The solid plate was ablated under low vacuum, stagnant, and flowing helium conditions to determine if the helium carrier gas was a source of oxidation. A plot of the peak height of the 777 and 845 nm oxygen lines versus time is shown in Figure 5.16. The two peaks are plotted to show that they track each other, indicating the signal is indeed from oxygen. Every point on the graph represents the spectra obtained from integrating over 7 laser pulses at 1 pps. The time at which each data point was taken is given to the minute after the start of the experiment and the graph is divided into sections (a to e) for the different experimental conditions.

At the start of the experiment, section (a) of Fig. 16, the ablation cell was sealed and under low vacuum, approximately 100 mTorr. The vertical arrows between two measurement points indicate the laser was fired 150 times over 3 seconds to clean the surface. After the second cleaning event, the oxygen signal was low and did not change over time. It may be inferred that the rate of removal of surface material by the laser at this point (specifically the number of oxygen atoms) was in equilibrium with the rate of oxidation of the surface. It is assumed that the laser removes unoxidized material below the surface oxide as well.

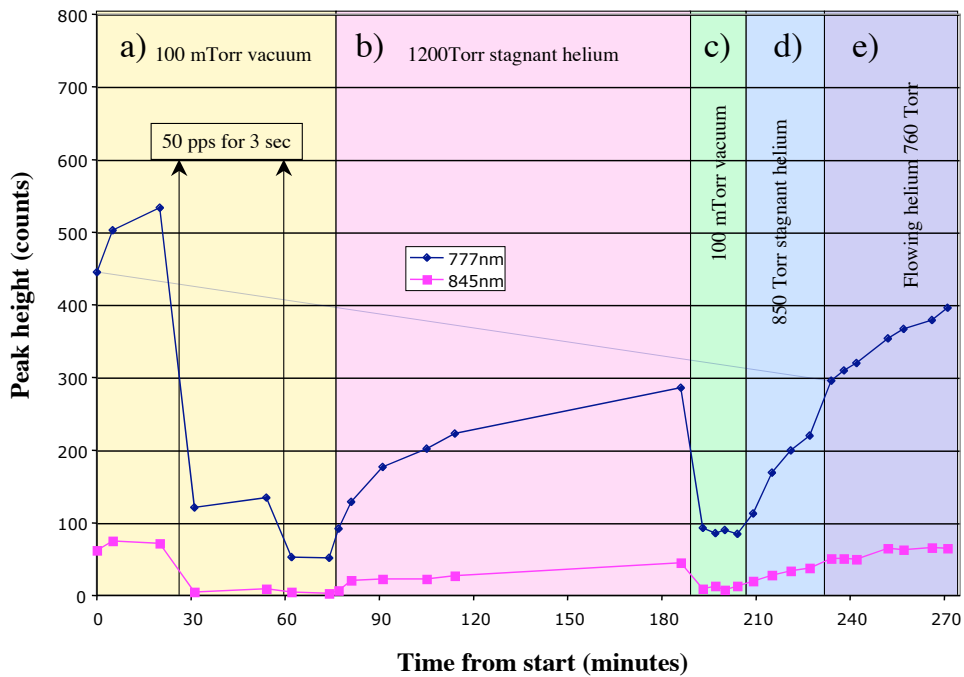


Figure 5.16 Plot of oxygen signal (peak height) from the laser ablation of a solid plate of Terfenol-D over time for different 99.99% helium background conditions. **a)** ablation cell under vacuum at ~100 mtorr. **b)** stagnant helium at 1200 Torr **c)** ablation cell again under vacuum **d)** stagnant helium at 850 Torr **e)** flowing helium at atmospheric pressure

At this point, section (b), the ablation cell was pressurized with 99.99% pure helium and a stagnant pressure of 1100 Torr was reached. The oxygen signal increased with each subsequent measurement, indicating an increase in the rate of oxidation (with respect to the rate of removal by the laser) of the surface in the presence of the helium gas. After about 110 minutes, the oxygen signal was still increasing but at a much lower rate.

The above sequence was repeated in sections (c) and (d), and similar results were obtained. Vacuum conditions generated a low oxygen signal while a static pressure of helium at about 850 Torr, caused a rise in the oxygen signal over time.

In section (e), helium was allowed to flow through the system at atmospheric pressure (760 Torr) in the same manner as during a LAM film deposition. This presented the surface of the Terfenol-D target with continuous, new helium gas (and its impurities). Subsequently, the oxygen signal increased above the stagnant helium level and at a faster rate than in the previous sections (b) and (d).

Qualitatively, atmospheric pressures of 99.99% pure helium did contribute to the oxidation of a surface of Terfenol-D and was worse in a flowing configuration as compared to a stagnant gas at the same pressure. The consequences of this will be discussed in the next chapter.

5.4 Data Summary

In summary, Terfenol-D feed particles were milled from pieces cut from a solid plate of Terfenol-D purchased from Etrema, Inc. The plate was also used in the deposition of thin films by PLD and in the spectroscopic studies of oxidation. The milled microparticles were used as feedstock material in the LAM process to create amorphous nanoparticles that were impacted on various substrates forming films.

These films were amorphous as determined by x-ray diffractometry (XRD), had compositions similar to the starting material, and showed an increase in oxygen content after 5 months of exposure to air. They were about 30% porous giving rise to an elastic modulus of about 14 GPa, half that of the starting material. Films showed saturation magnetization on the order of 5-10 emu/g (1/10 that of the stated value for Terfenol-D), and had magnetostriction coefficients on the order of 16 ppm. This is approximately 1/20 of the expected value of such a film.

Oxygen was detected in optical emission spectra of the ablation plasma, and it was determined that the signal originated from the surface of the microparticles as opposed to the background gas. However, 1 atm of 99.99% pure helium did contribute to the oxidation of a test surface of Terfenol-D between laser pulses as it was being ablated.

6

Discussion

Great care was taken to adapt the LAM process to an UHV compatible system, and prevent oxidation of the nanoparticles and films of supersonically impacted nanoparticles. In addition, a thin film gold encapsulation layer was used when higher environmental isolation was desired for the film. Unfortunately, the oxidation may have already occurred before the deposition of the gold film since the measured level of magnetostriction was always well below that expected of iron–rare earth films. In this concluding chapter, a discussion of the data that were obtained by the methods and techniques described in Ch. 4 attempts to explain this observed behavior. The source of the oxygen signal in the ablation plasma is considered first followed by the magnetostriction curve of the LAM films. From the discussion, future work is suggested, and finally a summary and conclusions of the research are given.

6.1 Oxidation

6.1.1 Background Gas Impurities

Optical spectroscopy of the ablation plasma (shown in chapter 5) revealed the existence of oxygen despite careful measures taken to use UHP (ultra high purity) helium and UHV (ultra high vacuum) procedures (e.g. metal seals for gas line connections). The experiments with ablating solid Terfenol-D in helium at atmospheric pressure showed that the surface does still oxidize to some degree between laser pulses. A calculation using the ideal gas law gives the order of impurities in 99.9995% pure (UHP) helium to be 10^{14} impurities/cm³ at room temperature and atmospheric pressure. In contrast, during film deposition by sputtering, the pressure is typically 6 orders of magnitude less than atmospheric pressure and consequently the impurities number about 10^8 impurities/cm³.

In the normal operating regime of the LAM process, a microparticle aerosol having an aerosol density on the order of 10^5 microparticles/cm³ is directed through the ablation region, though that can vary depending on feed particle size, gas flow rates, and other conditions. If all the impurities in the background helium contributed one oxygen atom, and all oxygen atoms were scavenged by the atomic metal vapor as it cools and forms nanoparticles, or by the resulting nanoparticles in the second it takes to travel to the supersonic nozzle and be impacted into a film, less than 0.5% of all rare earth elements would be oxidized. This is for starting Terfenol-D feedstock particles with a diameter of 3 μm . However if the same 10^5 microparticles /cm³ were only

0.3 μm in diameter, as do exist in large numbers according to Fig 3.3, there would be more than one oxygen atom for every atom in the microparticle, including iron. The material would be completely oxidized. Due to the fact that there exists some small magnetostriction, it is most likely that the microparticles that are actually aerosolized cover a range of sizes between these two cases such that there is enough oxygen to significantly oxidize the rare earth elements. The rare earths are far more reactive than the iron and are preferentially oxidized. Additionally the fluidized bed aerosol generator is known to break up loose agglomerates and preferentially feed the smaller particles. Thus, initially, the aerosolized and ablated microparticles will tend to be the smaller end of the feedstock size distribution with a shift toward fewer but larger particles later in time as the fine particles are exhausted. Figure 6.1 shows a plot of the calculated ratio of oxygen to iron due to background impurities for different starting iron microparticle diameters and aerosol densities assuming 99.9995% pure helium at atmospheric pressure.

Hence, it is preferable to operate in a high aerosol density of large microparticles to increase the mass density or material loading of the aerosol and reduce the impact of the background impurities. However, there are caveats. It is important to note that increasing the aerosol density tends to introduce turbulence in the ablation region. This leads to coalescence of smaller nanoparticles into larger particles and/or agglomeration of the nanoparticles, both of which are detrimental to the supersonic impaction process. From the model of Huang, et al., acceleration of larger particles (>20 nm) becomes

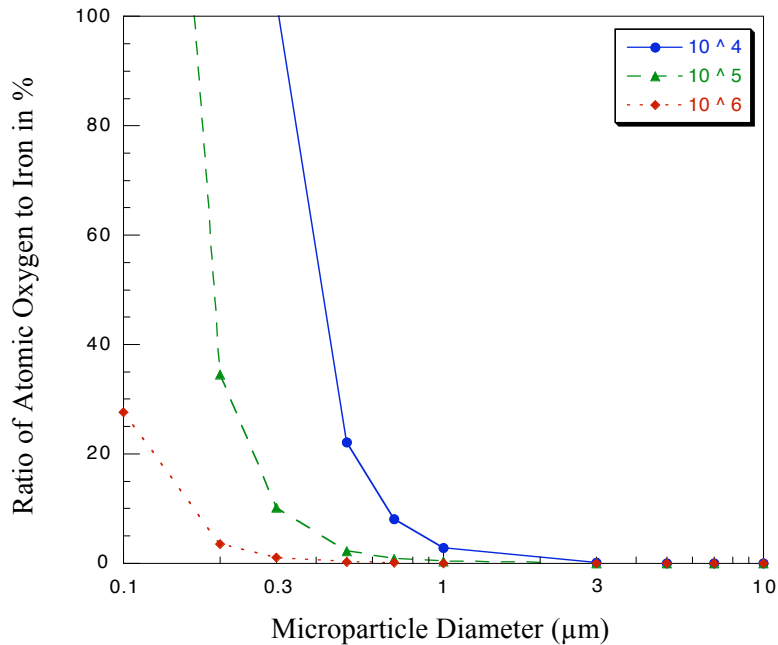


Figure 6.1 Calculated oxygen to iron ratio in percent due to oxygen impurities in the background helium. The different curves represent different aerosol densities : (blue circles) 10^4 particles/cm³, (green triangles) 10^5 particles/cm³, (red diamonds) 10^6 particles/cm³

difficult and the impaction velocity (and hence energy) of these larger particles decreases. Agglomerates tend to be fractal- or snowflake-like and the impaction energy goes into breaking the bonds between particles rather than into heating of the particles themselves. This reduces the ability to create a dense and monolithic film. In addition, increasing the size of the feedstock particles makes them more difficult to aerosolize,

reducing the aerosol density, and after a certain diameter, the larger particle size begins to hinder the shockwave efficiency and nanoparticle formation mechanism of the LAM process [37].

6.1.2 Microparticle Surface Oxide

From the laser ablation of a solid Terfenol-D target in air (Ch. 5), it was shown that the spectroscopic oxygen signal in the ablation comes from the surface material of the target as opposed to the surrounding gas. Hence, the oxygen signal from the ablation of microparticles is due to the surface oxide on the microparticles. Normally, the surface oxide would contribute only a small amount of oxygen assuming the microparticles are of the order of 2-5 μm in diameter. Figure 6.2 shows a calculation of the ratio of oxygen atoms to iron atoms in percent as a function of the iron microparticle diameter for different thicknesses of surface oxide. The model assumes Fe_2O_3 oxide on a pure iron particle. For example, a 10 nm Fe_2O_3 surface oxide layer on a 3 μm diameter particle represents an atomic ratio of oxygen to iron of 1 percent, while the same oxide on a 0.3 μm diameter particle has an oxygen to iron ratio of 12 percent. Including the aerosol density of 10^5 microparticles/ cm^3 , particles with a diameter of 3 μm , and a 10 nm surface oxide will add an additional 1.5×10^{14} oxygen atoms/ cm^3 to the impurities. The same aerosol density, but with 0.3 μm particles and a 10 nm surface oxide, contributes only 3×10^{12} additional oxygen atoms/ cm^3 though a correspondingly fewer iron atoms as well.

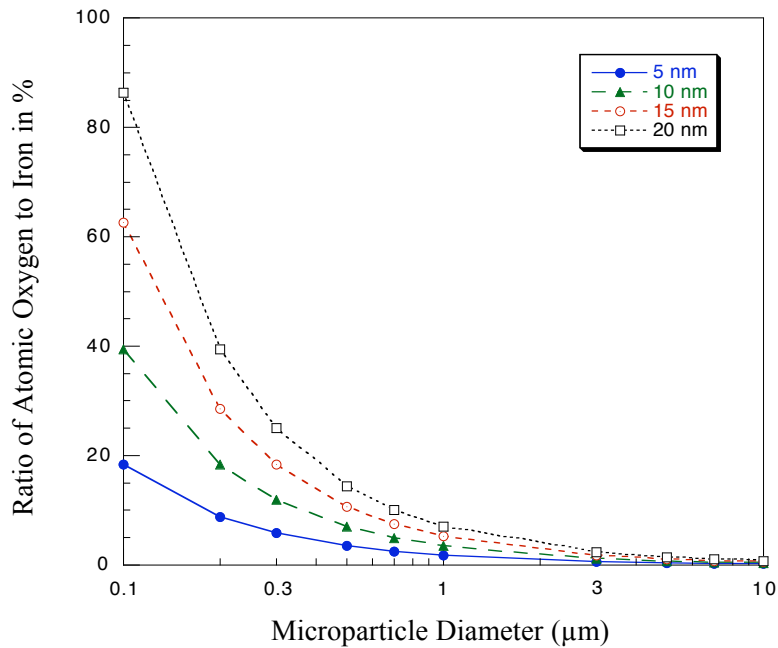


Figure 6.2 Calculated oxygen to iron ratio in percent due to a surface oxide on iron microparticles at an aerosol density of 10^5 particles/cm³. The different curves represent different oxide thicknesses : (blue filled circles) 5 nm thick surface oxide layer, (green triangles) 10 nm, (red open circles) 20 nm, (black open squares) 15 nm.

Contrary to the background gas source of oxygen, changing the number of microparticles/cm³ changes the number of impurity atoms per cubic centimeter but also changes the total number of atoms from the constituent microparticle. It is the oxide thickness and the diameter of the microparticle that determine the oxygen to metal ratio regardless of the number density of microparticles. Thus, it is again preferable (and

with the same caveats as before) to use large diameter feedstock microparticles with little or no surface oxide in order to minimize the number of oxygen impurities.

Figure 6.3 plots the oxygen to iron atomic ratio in percent for different diameter microparticles due to the combined effect of a surface oxide layer on the microparticles and impurities in the background gas. The assumptions are that the background gas is 99.9995 % pure at 1 atm pressure, and the oxide (Fe_2O_3) thickness of the microparticles is 10 nm.

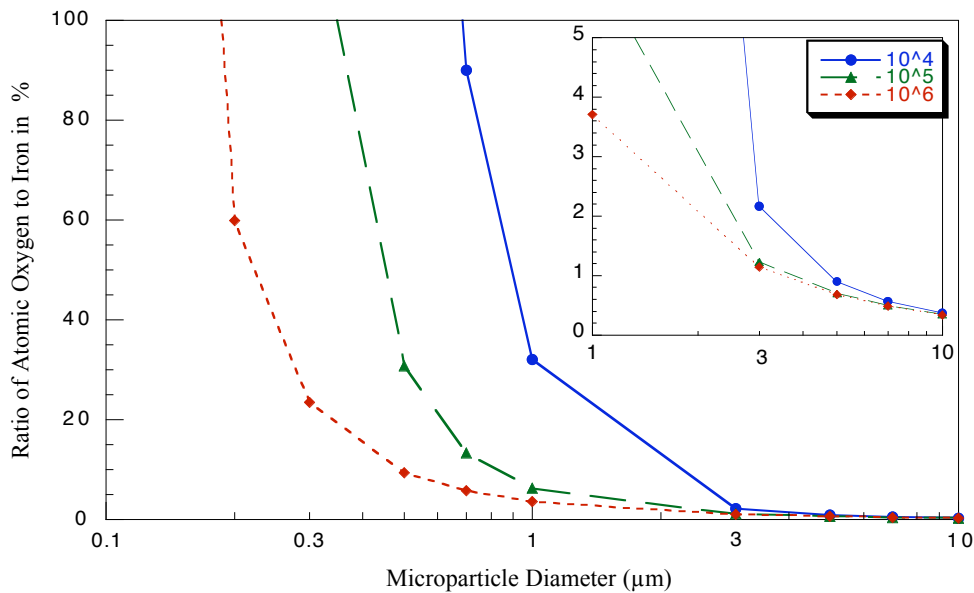


Figure 6.3 Ratio of total oxygen to iron in percent for different microparticle aerosol densities: (blue circles) 10^4 particles/cm³, (green triangles) 10^5 particles/cm³, (red diamonds) 10^6 particles/cm³. This total includes both the background gas impurities from 1 atm of 99.9995% pure helium and a surface oxide Fe_2O_3 10 nm thick.

From the figure it can be seen that nanoparticles made from microparticles with diameters below 3 μm are subjected to large numbers of impurities (oxygen), particularly for low aerosol densities. In the aerosol density range of 10^4 to 10^6 microparticles/ cm^3 , only ablation of microparticles larger than 5 μm in diameter results in impurities below 1 atomic % (cf. inset plot of Fig. 6.3). This is of course constrained to the assumptions of the model but does provide a guide to the size range of acceptable microparticle feedstock diameters. It also makes clear that microparticles with diameters as low as 0.3 μm are unacceptable as feedstock in the LAM process except at the highest aerosol densities and only without a native oxide surface layer. In fact, these particles are poor feedstock for the LAM process in general, as the surface evaporation mode of the nanoparticle size distribution begins to dominate at small feedstock particle sizes [38]. This generates larger nanoparticles and can lead to composition variations due to differences in the boiling points of the constituent elements [39].

Having determined that the Terfeonol-D microparticles are in fact oxidized, the question becomes how and where did they become oxidized? From the experiments ablating a solid plate of Terfeonol-D in helium it is known that the surface does oxidize to an extent over time. It is possible that the microparticle surface oxidizes as the helium passes through and aerosolizes the microparticles, in which case, the amount of oxygen in the ablation plasma is equivalent to that described in section 6.1.1 above. However, experiments and observations were recently carried out during the grinding

and preparation of the powder feedstock that indicate the microparticles had a surface oxide before being placed in the aerosolizer.

Drie-Rite, a commercially produced desiccant (CaSO_4) which readily chemisorbs 6% of its dry weight in water, was introduced into the glove box where the solid Terfenol-D material was ground to a powder. Over a period of a few days, amounts of water in excess of 10 grams were removed multiple times during the experiment. Hence oxidation of the microparticles was taking place during milling in the glove box via water vapor as opposed to oxygen gas. This was evident in hindsight when grinding the material by hand. Fracturing a piece of Terfenol-D created a bright silver surface which when ground in a mortar and pestle, was a dull, brownish-black powder. It was discovered that the main source of water was paper used to line the inside of the glove box. The paper absorbed moisture from the air and was releasing it into the dry argon gas after being inserted into the glove box.

Because the glove box cannot support vacuum, nor be baked as vacuum chambers can be, a blower coupled to a stainless steel vessel containing approximately 1 kg of Drie-Rite was placed in the glove box (after removing the offending paper) to continuously circulate the argon through the desiccant. This facilitates the removal of any residual water and in particular water that enters the glove box adsorbed on the surface of utensils, containers, and the aerosol generator transfer chamber. Unfortunately a new set of LAM films from Terfenol-D microparticles has not yet been carried out at the time of this writing.

6.2 Future Work

In all of the work regarding Terfenol-D that was done for this research, the most overlooked, and in the author's opinion, the most influential aspect of the process was control over the microparticle feedstock. This includes control of the size distribution and morphology, contamination (oxidation in this case), and aerosol density in the laser ablation region. Hence any future work should address these issues, both in the understanding of their effects on the desired nanoparticles or deposited nanostructures, and in their control.

As a process improvement in the supersonic jet deposition part of the process, feedback control of the substrate speed from a measurement of the microparticle feedstock aerosol density would aid in the film uniformity over larger dimensions. In addition to improved film performance, the thicknesses of the films are often used in calculations and the accuracy of the results would improve.

Scientifically, supersonic jet deposition of magnetic nanoparticles in a strong magnetic field would be of interest, both in the resulting film properties and in the influence on the jet dynamics. In terms of Terfenol-D, high frequency excitation could be an interesting area of study. The fact that the nanoparticle impacted film is porous (the extent of which can be varied) changes not only the elastic modulus but the matching properties, similar to index matching in optics, due to the size of the nanostructure morphology compared to even high frequency acoustic wavelengths. In

addition, eddy current loss could be minimized by the porosity and small grain size as both affect electrical conductivity.

6.3 Conclusions

Films were deposited from supersonic impaction of nanoparticles generated by the laser ablation of Terfenol-D microparticle aerosols. The films were found to be amorphous as determined by x-ray diffraction. Through implementation of a method that used the difference in coefficients of thermal expansion between the film and substrate, the films were found to have an elastic modulus approximately half that commonly reported for bulk Terfenol-D due to a porosity of 20 to 30%. Magnetostriction was weak compared with similar films deposited by other methods. To increase the sensitivity of the measurement and reduce the verification time, a variable magnetic field source using only permanent magnets, was designed and constructed. The weak magnetostriction was attributed to oxidation of the deposited material. Through spectroscopic experiments, it was found that the oxidation of the material occurred in the ablation and nanoparticle formation region of the LAM process, even before impaction into a film. The source of oxygen was attributed to both the impurities in the background gas and on the surface of the feedstock microparticles, and simple calculations corroborated these sources of oxygen. From the calculations, a microparticle diameter of 5 μm is suggested as the minimum diameter to ensure a ratio of less than 1 % of oxygen contaminants to metal for aerosol densities between 10^4 and

10^6 particles/cm³. The main source of oxygen on the surface (a surface oxide layer) of the microparticles was found to be water vapor in the glove box where the feedstock microparticles of Terfenol-D were ground.

It is worth noting that the findings here do not preclude the use of the LAM method and subsequent nanoparticle supersonic impaction for the formation of magnetostrictive materials. However, certain precautions must be taken in the choice of microparticle feedstock size and careful attention must be paid to all sources of oxygen, including prevention of oxidation after exposure of the sample to atmosphere. In addition suitable diagnostics for the detection of oxygen (for example, spectroscopy of the ablation plasma) should be implemented, and monitored in real-time if possible.

References

- [1] A.S. Edelstein and R.C. Cammarata, eds., Nanomaterials: Synthesis, Properties, and Applications. Philadelphia: Institute of Physics Pub., 1996.
- [2] Herzer, G., “Soft magnetic nanocrystalline materials,” *Scripta Metallurgica et Materialia*, vol. 33, no. 10, pp. 1741-1756, 1995.
- [3] Moran, M. J. and Shapiro, H. N., Fundamentals of Engineering Thermodynamics, 5th ed., New York: J. Wiley & Sons, 2004.
- [4] O’Brien, D.T., “Deposition and Characterization of Nanostructured Thick Films, Thesis (M.S. in Engineering), University of Texas at Austin, 2003.
- [5] Koper, O., and Klabunde, K. J., “Nanoparticles for the destructive sorption of biological and chemical contaminants,” U.S. Patent No., 6,057,488, 2000.
- [6] B. Weiser, H. Pfützner, and J. Anger, “Relevance of Magnetostriction and Forces for the Generation of Audible Noise of Transformer Cores,” *IEEE Trans. Magn.*, vol. 36, no. 5, p. 3759, September 2000.
- [7] Taguchi, S., Yamamoto, T., and Sakakura, A., “New Grain-Oriented Silicon Steel with High Permeability ORIENTCORE HI-B,” *IEEE Trans. Magn.*, vol. MAG-10, no. 2, pp. 123-127, June 1974.
- [8] Kittel, C., Introduction to Solid State Physics, 7th ed., New York: J. Wiley & Sons, 1996.
- [9] Engdahl, G., Handbook of Giant Magnetostrictive Materials, San Diego, California: Academic Press, 2000.
- [10] Clark, A. E., “High Power Magnetostrictive Materials from Cryogenic Temperatures to 250 C,” *Mat. Res. Soc. Symp. Proc.*, vol. 360. pp. 171-182, 1995.
- [11] Hadjipanayis, G. C., “Nanophase Hard Magnets,” *Journal of Magnetism and Magnetic Materials*, vol. 200, pp. 373-391, 1999.

- [12] Trémolet de Lacheisserie, E., Gignoux, D., and Schlenker, M., editors, Magnetism I - Fundamentals., The Netherlands: Kluwer Academic Publishers, 2002.
- [13] Snodgrass, J. D., and McMasters, O. D., "High Performance Rare Earth Transition Metal Magnetostrictive Materials," U.S. Patent no. 6,273,966, 2001.
- [14] Kim, D. H., Kwon, O. Y., Kim, J. C., Lee, Z. H., "Effect of Oxygen Impurity on Magnetostriction of Directionally Solidified Tb_{0.3}Dy_{0.7}Fe_{1.8}," *IEEE Trans. Magn.*, vol. 40, no. 4, pp. 2781-2783, 2004.
- [15] Quandt, E., Gerlach, B., and Seemann, K., "Preparation and Applications of Magnetostrictive Thin Films," *J. Appl. Phys.* vol. 76, no. 10, pp.7000-7002, 1994.
- [16] van Dover, R. B., Gyorgy, R.P., Frankenthal, M. H., and Siconolfi, D. J., "Effect of Oxidation on the Magnetic Properties of Unprotected TbFe Thin Films," *J. Appl. Phys.*, vol. 59, no. 4, pp. 1291-1296, 1986.
- [17] M.F. Becker, J.R. Brock, J.W. Keto, "Process for the production of nanoparticles," U.S. Patent No. 5,585,020, 1996.
- [18] C.B. Juang, H. Cai, M. F. Becker, J. W. Keto, and J. R. Brock, "Synthesis of nanometer glass particles by pulsed-laser ablation of microspheres," *Appl. Phys. Lett.*, vol. 65, no. 1, pp. 40-42., 1994.
- [19] W. T. Nichols, J. W. Keto, D. E. Henneke, J. R. Brock, G. Malyavanatham, M. F. Becker, H. D. Glicksman, "Large-scale production of nanocrystals by laser ablation of microparticles in a flowing aerosol," *App. Phys. Lett.*, vol. 78, no. 8, 2001.
- [20] J. Lee, M. F. Becker, J. W. Keto, "Dynamics of laser ablation of microparticles prior to nanoparticle generation," *J. Appl. Phys.*, vol. 89, no. 12, pp 8146-8152, 2001.
- [21] W. T. Nichols, G. Malyavanatham, D. E. Henneke, J. R. Brock, M. F. Becker, J. W. Keto, "Bimodal nanoparticle size distributions produced by laser ablation of microparticles," *J. Nanoparticle Research*, vol. 4, pp. 423-432, 2002.

- [22] H. Hsieh, R. Averback, H. Sellers, C. Flynn, "Molecular-dynamics simulations of collisions between energetic clusters of atoms and metal substrates," *Phys. Rev. B*, vol. 45, no. 8, pp 4417-4430, 1992.
- [23] Huang, C., Nichols, W. T., O'Brien, D. T., Becker, M. F., Kovar, D., Keto, J. W., "Supersonic Jet Deposition of Silver Nanoparticle Aerosols: Correlations of Impact Conditions and Film Morphologies," *J. Appl. Phys.*, accepted for publication, 2006.
- [24] H. Haberland, Z. Insepov, M. Moseler, "Molecular-dynamics simulation of thin-film growth by energetic cluster impact," *Phys. Rev. B*, vol. 51, no. 16, pp 11061-11067, 1995.
- [25] Trémolet de Lacheisserie, E., and Peuzin, J.C., "Magnetostriction and Internal Stresses in Thin Films: the Cantilever Method Revisited," *J. Magn. Magn. Mater.*, vol. 136, pp. 189-196, 1994.
- [26] Timoshenko, S., "Analysis of Bi-Metal Thermostats," *J. Opt. soc. Am.*, vol. 11, no. 3, pp. 233-255, 1925.
- [27] Chu, W., Mehregany, M., Mullen, R.L., "Analysis of Tip Deflection and Force of a Bimetallic Cantilever Microactuator," *J. Micromech. Microeng.*, vol. 3, pp. 4-7, 1993.
- [28] McAdam, G. D., *J. Iron Steel Inst.*, vol. 168, p. 346, 1951, in J. S Hirschhorn, Introduction to Powder Metallurgy. New York: The Colonial Press, Inc., 1969.
- [29] Halbach, K., "Design of Permanent Multipole Magnets with Oriented Rare Earth Cobalt Material," *Nucl. Instrum. Methods*, vol 169, no. 1, pp. 1-10, 1980.
- [30] Cugat, O., Byrne, R., McCaulay, J. and Coey, J. M. D., "A Compact vibrating-sample Magnetometer with a Variable Permanent Magnet Flux Source," *Rev. Sci. Instrum.*, vol. 65, no. 11, pp. 3570-3573, 1994.
- [31] Personal communication with Rory Murphy of Magnetic Solutions, Ltd., Dublin, Ireland, January 2005.
- [32] Cugat, O., Hansson, P., Coey, J. M. D., "Permanent Magnet Variable Flux Sources," *IEEE Trans. Magn.*, vol. 30, no. 6, pp. 4602-4604, 1994.

- [33] Cheng, Meng-Dawn, "Real-time Measurement of Trace Metals on Fine Particles by Laser-Induced Plasma Techniques," *Fuel Processing Technology*, vol 65, pp. 219-229, 2000.
- [34] Engdahl, G., Handbook of Giant Magnetostrictive Materials, San Diego, California: Academic Press, 2000.
- [35] Grundy, P.J., Lord, D. G., Williams, P.I., "Magnetostriction in TbDyFe Thin Films," *J. Appl. Phys.*, vol. 76, no. 10, pp. 7003-7005, 1994.
- [36] Schatz, F., Hirscher, M., Schnell, M., Flik, G., Kronmuller, H., "Magnetic Anisotropy and Giant Magnetostriction of Amorphous TbDyFe Films," *J. Appl. Phys.*, vol. 76, no. 9, pp. 5380-5382, 1994.
- [37] Carranza, J. E., Hahn, D. W., "Assessment of the Upper Particle Size Limit for Quantitative Analysis of Aerosols Using Laser-Induced Breakdown Spectroscopy," *Anal. Chem.*, vol. 74, pp. 5450-5454, 2002.
- [38] Nichols, W. T., Malyavanatham, G., Henneke, D. E., Brock, J. R., Becker, M. F., Keto, J. W., "Bimodal nanoparticle size distributions produced by laser ablation of microparticles," *J. Nanoparticle Research*, vol. 4, pp. 423-432, 2002.
- [39] Malyavanatham, G., et al., "Thick films fabricated by laser ablation of PZT microparticles," *Journal of Materials Processing Technology*, vol. 168, pp. 273-279, 2005.

VITA

Daniel Thomas O'Brien was born in Story City, Iowa on November 17th, 1975, the son of Janet and Edward O'Brien. After completing high school at D. W. Daniel High School, Clemson, South Carolina, he entered Boston University in the fall of 1994. He received the degree of Bachelor of Science in January 1999 with a major in Electrical Engineering and a minor in Mathematics. In the fall of 1999 he entered the Graduate school at the University of Texas at Austin and received the Master of Science in Engineering degree from UT in May of 2003. Daniel and Ella Marion Sciamma were married June 10, 2006, in Bourg-d'Oisans, France.

Permanent Address: 1302 West 24th St. #202
 Austin, TX 78705

This dissertation was typed by the author.